Monthly Notices
of the
ROYAL ASTRONOMICAL SOCIETY

MNRAS **463,** 771–793 (2016)
Advance Access publication 2016 August 15

doi:10.1093/mnras/stw1969

ExoMol line lists – XVIII. The high-temperature spectrum of VO

Laura K. McKemmish,* Sergei N. Yurchenko and Jonathan Tennyson*

Department of Physics and Astronomy, University College London, Gower Street, WC1E 6BT London, UK

Accepted 2016 August 4. Received 2016 July 21; in original form 2016 May 25

ABSTRACT

An accurate line list, VOMYT, of spectroscopic transitions is presented for hot VO. The 13 lowest electronic states are considered. Curves and couplings are based on initial *ab initio* electronic structure calculations and then tuned using available experimental data. Dipole moment curves, used to obtain transition intensities, are computed using high levels of theory (e.g. MRCI/aug-cc-pVQZ using state-specific or minimal-state complete active space for dipole moments). This line list contains over 277 million transitions between almost 640 000 energy levels. It covers the wavelengths longer than 0.29 μm and includes all transitions from energy levels within the lowest nine electronic states which have energies less than 20 000 cm^{-1} to upper states within the lowest 13 electronic states which have energies below 50 000 cm^{-1}. The line lists give significantly increased absorption at infrared wavelengths compared to currently available VO line lists. The full line lists is made available in electronic form via the CDS database and at www.exomol.com.

Key words: molecular data – opacity – astronomical data bases: miscellaneous – planets and satellites: atmospheres – brown dwarfs – stars: low-mass.

1 INTRODUCTION

Vanadium oxide (VO) plays an important role in astrophysical chemistry, particularly of cool stars, and is expected to also be present in brown dwarfs and hot Jupiter exoplanets. However, no comprehensive, high-quality line list has been published for this molecule, limiting the potential information that can be obtained. The ExoMol project (Tennyson & Yurchenko 2012, 2014) aims to produce high-temperature line lists of spectroscopic transitions for key molecular species likely to be significant in the analysis of the atmospheres of extrasolar planets and cool stars. The molecular data are crucial for accurate astrophysics models of the opacity, as discussed by Sharp & Burrows (2007) and Bernath (2009), and the spectroscopy of the object. However, from a chemistry perspective, vanadium is a transition metal in terms of its electronic structure and spectroscopic properties. This makes the electronic structure calculations much more difficult and gives higher uncertainties (Tennyson et al. 2016a).

VO absorption bands are generally present in cool late M class stars with effective temperature on order of 2500–3000 K, mass less than 0.1 $M_\odot$ and are also expected to be observed in hot Jupiter exoplanets (Fortney et al. 2008). VO is generally present simultaneously with TiO and has similar spectroscopic and thermodynamic properties, though its abundance is about an order of magnitude less than TiO. VO tends to be more important in classifying slightly cooler (i.e. late) M dwarfs (Kirkpatrick et al. 1993; McGovern et al. 2004). VO is one of the dominant species in the spectra of young hot brown dwarfs (McGovern et al. 2004; Kirkpatrick et al. 2006; Peterson et al. 2008).

The A–X transition of VO, which occurs at approximately 1.05 μm in the infrared, was first observed in the red giant Mira-type variable stars Mira Ceti and R Leonis by Kuiper, Wilson & Cashman (1947), and subsequently studied more extensively by Keenan & Schroeder (1952), Spinrad & Younkin (1966), Wing, Spinrad & Kuhi (1967), Spinrad & Wing (1969), Alvarez & Plez (1998) and Castelaz, Luttermoser & Piontek (2000). VO has also been observed in M red-dwarf stars (Alvarez & Plez 1998; Bernath 2009; Rajpurohit et al. 2014). Molecular lines of VO have been detected in sunspot umbral spectra (Sriramachandran et al. 2008). Désert et al. (2008) found non-definitive evidence for VO in the atmosphere of the hot Jupiter HD209458b. Tentative detection of VO and TiO in the hot atmosphere of the hot exoplanet WASP-121b were recently reported by Evans et al. (2016).

There has been considerable recent debate (Spiegel, Silverio & Burrows 2009; Bowler et al. 2010; Fortney et al. 2010; Madhusudhan & Seager 2010; Huitson et al. 2012; Gibson et al. 2013; Parmentier, Showman & Lian 2013; Spiegel & Burrows 2013; Agúndez et al. 2014; Haynes et al. 2015; Hoeijmakers et al. 2015; Schwarz et al. 2015; Wakeford & Sing 2015) about a possible temperature inversion in hot Jupiters, potentially caused by the presence of TiO and VO. Hoeijmakers et al. (2015) highlight the need for more accurate line lists to resolve this issue; though they specifically mention TiO in this paper, VO usually coexists, although it is generally thought to have a lower abundance. Line lists for TiO (Plez 1998; Schwenke 1998; Ryabchikova et al. 2015), despite their shortcomings, are still significantly more developed than those for VO.

Kurucz (2011) and Plez (1999) have both circulated VO line lists. Both these line lists contained only transitions in the main

*E-mail: laura.mckemmish@gmail.com (LKM); j.tennyson@ucl.ac.uk (JT)

A–X, B–X and C–X bands (in particular, no infrared X–X transitions were included). These line lists have been used extensively in stellar and planetary models. Burrows, Hubbard & Lunine (1989) give an early study based on a simple model atmospheres incorporating TiO and VO opacities. In particular, VO is an important component of model atmospheres for M dwarfs (Allard & Hauschildt 1995; Rajpurohit et al. 2012, 2014). The more complex T Tauri atmosphere models have also incorporated VO absorption bands (Herczeg & Hillenbrand 2014).

A good VO line list is especially important in light of the new generation of proposed and planned satellites with the ability to take high-quality spectra of hot Jupiters. These are required both for missions purpose-designed for studying exoplanet spectroscopy (Tinetti et al. 2011, 2012; Tennyson & Yurchenko 2016) or more general purpose satellites such as *James Webb Space Telescope* which will also have the capability to study atmospheres of hot Jupiters in 0.6–28 μm region (Beichman et al. 2014; Barstow et al. 2015; Wakeford & Sing 2015).

VO is generally critical in modelling oxygen-rich astronomical objects with temperatures between 1500 and 3000 K: at lower temperatures, it condenses to more complex oxides while at higher temperatures it partially dissociates. VO may continue to be a non-negligible source of opacity and absorption up to 5000 K; therefore, we aim for a 90 per cent complete line list up to this temperature. The resulting line list should automatically be valid for any lower temperatures.

Due to its astronomical importance in the spectroscopic analysis of M dwarfs, the spectroscopy of diatomic VO has been well studied experimentally (Kasai 1968; Laud & Kalsulka 1968; Richards & Barrow 1968a,b; Harrington & Nicholls 1969; Cheung et al. 1981; Hocking, Merer & Milton 1981; Cheung, Hansen & Merer 1982a; Cheung, Taylor & Merer 1982b; Merer et al. 1987; Merer 1989; Huang, Merer & Clouthier 1992; Cheung et al. 1994; Adam et al. 1995; Ram et al. 2002; Ram & Bernath 2005; Hopkins, Hamilton & Mackenzie 2009). A good summary of previous experimental results is given by Miliordos & Mavridis (2007) and Hopkins et al. (2009). Generally, only the ground and first vibrational energy levels are well characterized for observed electronic states. Fortunately, transitions between quartet and doublet electronic states have been observed; this enables the relative positioning of the quartet and doublet manifold to be fixed with reasonably accuracy (limited by the fact that the absolute value of some spin–orbit terms is unknown experimentally).

The dipole moment of the ground state has been measured by Suenram et al. (1991). There is no information on the transition dipole moments of VO. However, lifetime measurements for levels in the A, B and C states were performed by Karlsson et al. (1997).

The spectroscopy of VO has also been well studied theoretically (Carlson & Moser 1966; Wolf, Farberov & Shirokovskii 1977; Bauschlicher & Langhoff 1986; Dolg et al. 1987; Bauschlicher & Maitre 1995; Bakalbassis et al. 1996; Bridgeman & Rothery 2000; Broclawik & Borowski 2001; Dai et al. 2003; Pykavy & van Wullen 2003; Mackrodt, Middlemiss & Owens 2004; Quan et al. 2006; Yao et al. 2007; Bande & Lüchow 2008; Quan et al. 2008; Kulik & Marzari 2010; Pradhan et al. 2011). However, the challenging nature of theoretical treatments of excited states in transition metal diatomics means that achieving quantitative accuracy is very difficult, particularly for excitation energies (Tennyson et al. 2016a). Generally, multireference configuration interaction (MRCI) approaches are essential.

The most detailed *ab initio* electronic structure study was performed by Miliordos & Mavridis (2007), who looked at the lowest

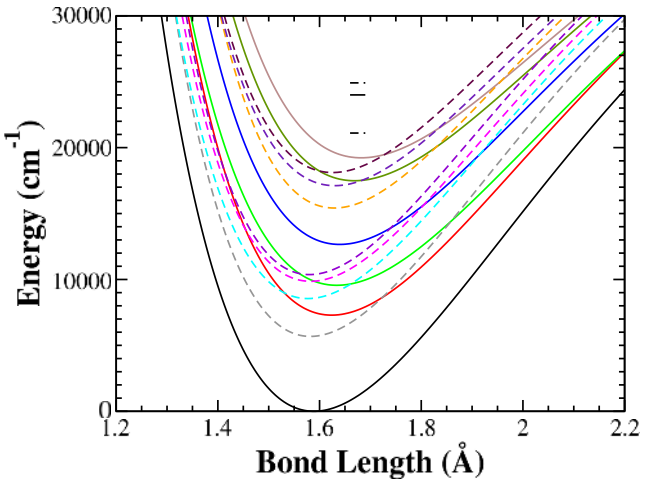

Figure 1. Potential energy curves. Curves in ascending order are: solid; X $^4\Sigma^-$, A′ $^4\Phi$, A $^4\Pi$, B $^4\Pi$, C $^4\Sigma^-$, D $^4\Delta$; dashed; a $^2\Sigma^-$, b $^2\Gamma$, c $^2\Delta$, d $^2\Sigma^+$, e $^2\Phi$, f $^2\Pi$, g $^2\Pi$. The short horizontal lines above the full curves are indicative of the next highest known quartet (solid) and doublet (dashed) states based on experimental data; there are many extra doublets believed to exist above 20 000 cm^{-1} not shown on this graph.

nine electronic states, and also reviewed previous theoretical studies. The quality of these calculations is high, but quantitative results are only given for equilibrium values.

Another important study was performed by Hübner, Hornung & Himmel (2015), who calculated the energetics of a much larger number of electronic states, but did not consider dipole moment or spin–orbit couplings (except for the X equilibrium dipole moment). They investigate the effect of including 3p correlation on the internally-contracted MRCI (icMRCI) results; however, the accuracy of the potential energy surface parameters does not show significant (if any) improvement. Their icMRCI calculations incorrectly predict the ordering of the C $^4\Sigma^-$ and D $^4\Delta$ states; we find similar difficulties in reproducing the correct ordering of these states.

The goal of this paper is to produce a comprehensive line list for the main isotopologue of VO accounting for all of the lowest 13 electronic states of VO.

The structure of this article is as follows. In Section 2, the spectroscopic model for VO is developed. In Section 3, the line list for VO, named VOMYT, is constructed based on the spectroscopic model developed here and earlier (McKemmish, Yurchenko & Tennyson 2016). In Section 4, we compare cross-sections using the new VOMYT line list against laboratory, observational, and previous line list spectra.

2 CONSTRUCTING THE SPECTROSCOPIC MODEL FOR VO

2.1 General considerations

Astrophysically, vanadium is predominantly (>99.7 per cent) in one isotopic form, its only stable isotope, ^{51}V.

There are three main electronic systems in VO; the A–X, B–X and C–X bands with origin (0,0) bands starting around 1.05 μm (9500 cm^{-1}), 0.79 μm (12 600 cm^{-1}) and 0.57 μm (17 400 cm^{-1}), respectively.

However, VO, like most transition metal diatomics, has a large number of low-lying electronic states, as shown in Fig. 1. The

Table 1. Specifications for extended Morse oscillator parameters (see equation 1) for the fitted potential energy curves in DUO. The dissociation energy, D_e, is 52 288.4 cm^{-1} and the reduced mass of $^{51}V^{16}O$ is 12.172 961 18 Da.

State	Morse parameters					Properties
	T_e (cm^{-1})	R_e (Å)	b_0	b_1	b_2	ω_e (cm^{-1})
X $^4\Sigma^-$	0.000	1.589 443	1.879 74	0	0	1011.8
A′ $^4\Phi$	7293.270	1.622 990	1.895 29	0	0	946.4
A $^4\Pi$	9561.867	1.633 621	1.8200*	0	0	890.3
B $^4\Pi$	12 655.372	1.640 253	1.947 33	0	0	912.4
C $^4\Sigma^-$	17 487.690	1.670 620	1.946 74	−0.359	0.540	864.9
D $^4\Delta$	19 229.786	1.683 170	1.965 00	0.060	0.900	840.9
a $^2\Sigma^-$	5630.00*	1.582 00*	2.0100*	0	0	1041.7
b $^2\Gamma$	8551.49*	1.577 00*	2.0900*	0	0	1009.0
c $^2\Delta$	9860.107	1.582 247	2.075 38	0	0	1006.1
d $^2\Sigma^+$	10 343.630	1.578 560	2.161 31	0	0	1041.7
e $^2\Phi$	15 440.547	1.628 968	2.0900*	0	0	985.2
f $^2\Pi$	17 115.919	1.629 330	2.121 46	0.226	0.471	937.2
g $^2\Pi$	18 108.500	1.635 810	2.176 48	1.157	−1.850	947.5

∗: fixed based on theory or low-resolution experiment.

relative energy positioning and identity of the 13 lowest electronic states (pictured) are reasonably well established by current experimental and theoretical evidence. We consider these 13 states, six quartet states and seven doublet states, in our spectroscopic model of VO; the final parameters of these states in terms of extended Morse oscillators (EMOs) are given in Table 1 for reference, with detailed equations later in the manuscript.

Hübner et al. (2015) considered a larger number of electronic states than we use in our model; this informs our considerations of the limitations of our 13 state electronic state spectroscopy model for VO. Specifically, we have included all nearby quartet states, but there are very many doublet states just about 20 000 cm^{-1} that will be involved in perturbations, spin–forbidden transitions and hot bands.

The results of Hübner et al. (2015) show that there is a significant energetic gap between these six quartet states and the next lowest quartet state (more than 12 000 cm^{-1}). This gives confidence that there will not be additional strongly allowed electronic transitions from the ground state in the visible region.

However, there are numerous nearby higher doublet states which will certainly affect the spectroscopy of VO by perturbing the quartet states, spin–forbidden transitions and hot bands. There are not sufficient experimental data to fit these extra states and the accuracy of *ab initio* electronic structure calculations for these high-lying levels is not sufficient for spectroscopic purposes. It is clear that our 13 state model will not produce a full picture of the visible absorption within the doublet manifold, especially not with spectroscopic accuracy. However, the transitions involving the doublets are likely to be relatively weak, since they are either spin–forbidden or originate from excited states lying at least 5000 cm^{-1} above the ground state. Therefore, their absorption will contribute predominantly to the underlying continuum of VO absorption rather than to the strong signature bands; this absorption (which will particularly affect the opacity of the atmosphere) is significantly easier to model and will be less affected by perturbations in the energy levels.

We use some of the Miliordos & Mavridis (2007) results for potential energy curves (PECs) as a source of data for our line list. In particular, we use their results to fit the PECs of the a $^2\Sigma^-$ and b $^2\Gamma$ states and also use their calculation of the diagonal spin–orbit splitting of the c $^2\Delta$ and e $^2\Phi$ state to fix the spin–orbit splitting of the c $^2\Delta$, e $^2\Phi$ and f $^2\Pi$ states (the relative size of the spin–orbit coupling is known from experiment, but not their absolute values). However, Miliordos & Mavridis (2007) did not consider dipole moment (diagonal or off-diagonal), spin–orbit or electronic angular momentum coupling curves. New calculations for these properties are presented here. The spin–orbit couplings in particular can drastically affect the energy levels of the molecule.

2.2 Methodology

2.2.1 *Electronic structure calculations*

We use high level *ab initio* electronic structure calculations for VO by McKemmish et al. (2016), which include consideration of both static and dynamic electron correlation. In brief, the electronic structure calculations for this molecule were generally performed using MOLPRO (Werner et al. 2012) with the icMRCI (Knowles & Werner 1988; Werner & Knowles 1988; Knowles & Werner 1992) level of theory with the large aug-cc-pVQZ basis set (Dunning 1989; Balabanov & Peterson 2005) which incorporates diffuse functions to accurately describe the electronically excited states. The orbitals used in the icMRCI calculation were obtained using state-specific (SS) or minimal-state (MS) complete active space self-consistent field (CASSCF) calculations.

The *ab initio* results are shown as data points in Figs 2–6. Note that the *ab initio* results often do not extend beyond about 1.8 Å. This is due to convergence difficulties associated with an ionic/covalent avoided crossing; even if calculations converged, the dipole moment obtained was often unpredictable and not smooth in this region. Changes in basis set and/or method did not significantly improve smoothness and convergence. Thus, we choose to use *ab initio* points only where the calculations were trusted and the curves are smooth for accurate calculation of absorption intensities below 5000 K. Smoothness is an essential feature of dipole curves if physically correct results are to be obtained (Tennyson 2014).

The *ab initio* electronic structure results obtained using the above methodologies are not continuous or on a sufficiently fine grid to be used directly by a nuclear motion code to compute rovibronic energies, wavefunctions and transition intensities. Therefore, we need to interpolate and extrapolate the *ab initio* results to form our final spectroscopic model for VO. Due to the small number of points, simple cubic spline gave unphysical curves, particularly for the dipole moments. We thus chose to fit to physically motivated

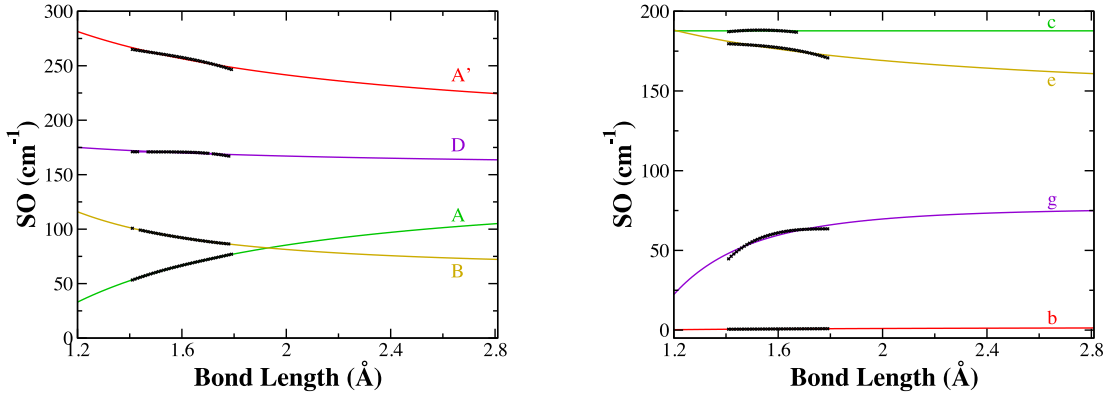

Figure 2. Diagonal spin–orbit coupling matrix elements. The darker small crosses are *ab initio* data from McKemmish et al. (2016). The lighter continuous lines are fitted curves as described in the text.

functional forms. The choice of functional form for each property of interest is discussed as relevant.

2.2.2 *Nuclear motion calculations*

DUO is a new program (Yurchenko et al. 2016b) written by the ExoMol group that solves the nuclear motion problem for diatomics with multiple highly coupled electronic states. The program DUO was used to produce rovibronic energy levels for VO. Input to this program were PECs, spin–orbit, spin–spin and spin–rotation coupling curves and dipole moment curves. DUO allows optimization of parameters or morphing of input curves to minimize the difference between the calculated and observed energy levels or transition frequencies that are provided.

2.2.3 *Collation and selection of experimental data*

The use of experimental data is imperative to ExoMol's methodology, particularly for molecules like VO where current *ab initio* electronic structure methods do not deliver sufficient accuracy as discussed by McKemmish et al. (2016) and Tennyson et al. (2016a) in detail. An important component of the line list generation is thus the collation and selection of a set of empirical energies and frequencies. The spectroscopic model has been refined to minimize the root mean squared deviation of the DUO predicted (calculated) energy levels and/or frequencies against the empirical (observed) values.

Tables 2–6 detail the major sources of experimental data used to construct the DUO spectroscopic model of VO.

Experimental transitions involving the doublet c $^2\Delta$, e $^2\Phi$, f $^2\Pi$ and g $^2\Pi$ states have been measured and used to construct model Hamiltonians fits for each spin-vibronic band. Some spin–forbidden doublet-to-quartet transitions have recently been observed (g $^2\Pi$–X $^4\Sigma^-$) by Hopkins et al. (2009) which are extremely useful in fixing the relative positions of the doublet and quartet states. However, these observed transitions do not quite provide sufficient information to determine the energy of all spin rovibronic bands relative to the zero of the X $^4\Sigma^-$ state. Specifically, there is a spectroscopic network connecting the {c $^2\Delta_{5/2}$, e $^2\Phi_{7/2}$, f $^2\Pi_{3/2}$ and g $^2\Pi_{3/2}$} states from the experiments reported by Merer et al. (1987), Ram et al. (2002) and Ram & Bernath (2005) via the observed g $^2\Pi_{3/2}$–X $^4\Sigma^-$ transition. This network can be connected to the ground state of VO. However, the spectroscopic network comprising {c $^2\Delta_{3/2}$, e $^2\Phi_{5/2}$, f $^2\Pi_{1/2}$} is not connected to g $^2\Pi_{1/2}$ and therefore also not to the X $^4\Sigma^-$ state and the absolute energy scale of VO. Nevertheless, the relative spin–orbit coupling matrix elements of the c $^2\Delta$, e $^2\Phi$ and f $^2\Pi$ are known from experiment, as detailed in Table 8. We can thus use a single magic number (Furtenbacher, Császár & Tennyson 2007) to connect the two spectroscopic networks. Based on *ab initio* electronic structure predictions by Miliordos & Mavridis (2007) and our own calculations, we choose this magic number by setting the spin–orbit coupling constant of the c $^2\Delta$ state to 180 cm^{-1}. Using this magic number and the spin–forbidden transitions, we can then set the absolute T_e for each doublet state. The model Hamiltonians given in the original experimental papers can then be used to produce empirical energies using PGOPHER (Western 2016). The J range of the energy levels we used was informed by the experimental data available in the original paper. The use of experimental energies from model Hamiltonian fits was judged sufficient for doublet states for two reasons: (1) the intensity of their transitions do not contribute significantly to the final absorption spectra and (2) the spin and rotational structure of doublet spectra are easier to fit (and hence more reliable) than for quartet spectra. Furthermore, manual checks of the reported frequencies against our calculated PGOPHER empirical energy levels showed good agreement. Table 2 details all the spin-vibronic bands of doublet states which we include in to refine the spectroscopic model. Note that we also include data on some d $^2\Sigma^+$ bands; these were not directly measured but inferred from perturbations to the B–X transitions.

For quartet states, we found some significant discrepancies between the calculated PGOPHER empirical energy levels and the frequencies reported in the original experimental manuscripts, particularly for the A–X transition. The origin of the differences could be typographic errors or different definitions of model Hamiltonian constants. Instead of retracing this error, we decided to use the frequencies directly as our source of experimental data. Assuming the model Hamiltonian representation of the X $^4\Sigma^-$ state (reasonable given the significant amount of data involving this state, and the consistency with latter combination differences), we produced empirical energy levels for the X $^4\Sigma^-$ state using PGOPHER. Based on these lower state energies, we could derive the upper state energies (e.g. the A $^4\Pi$, B $^4\Pi$ and C $^4\Sigma^-$ state energies) from the experimental frequencies based on the assignments given in the original paper. The 'combination differences' method was used in which an upper state energy was only trusted if two or more transitions gave the same energy for a particular upper state (within a threshold; here

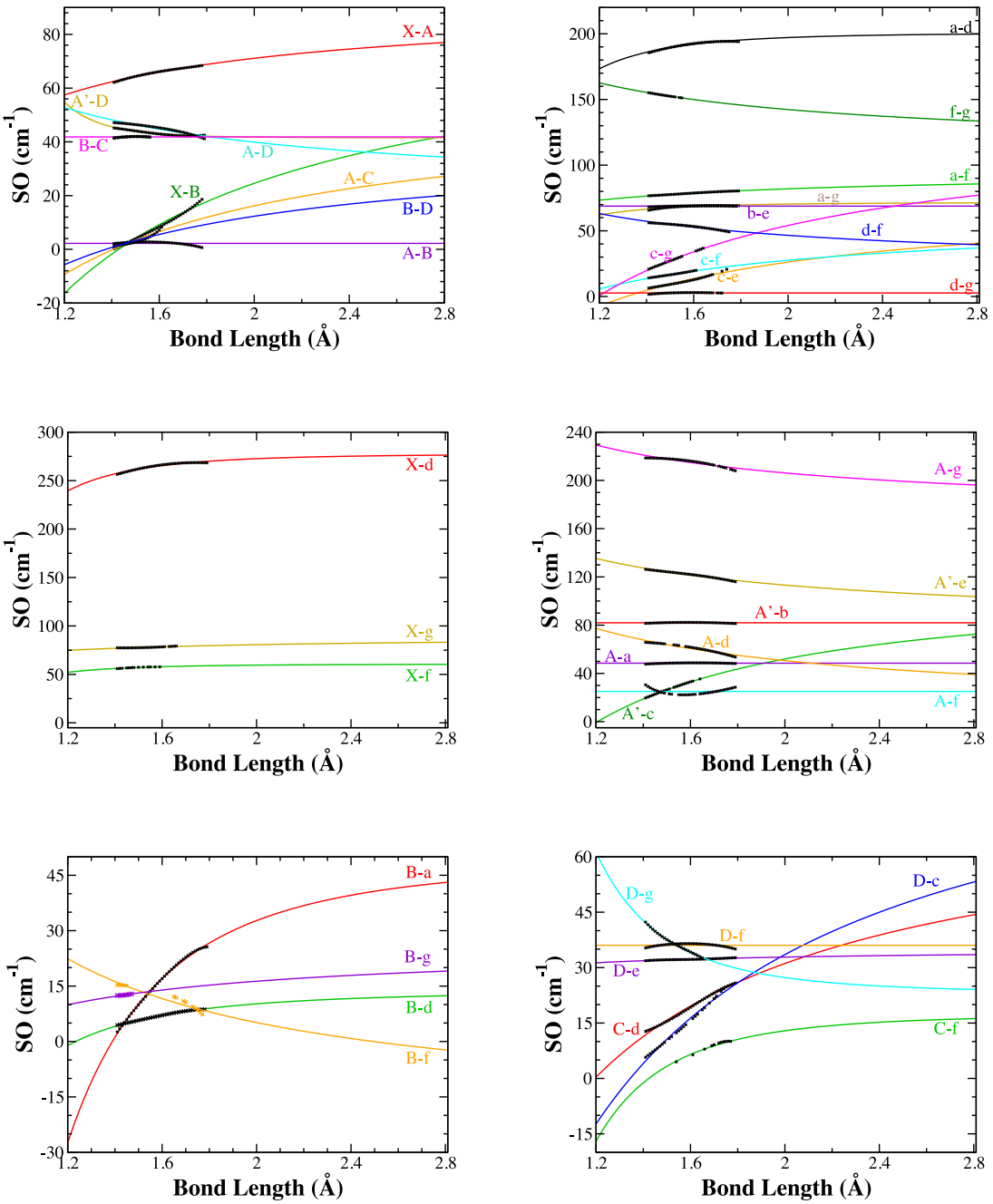

Figure 3. *Ab initio* off-diagonal spin–orbit coupling matrix elements calculated by McKemmish et al. (2016) in darker small crosses, and the fitted curves in lighter continuous curves.

selected to be the relatively loose 0.2 cm^{-1}). This process yielded a set of A $^4\Pi$, B $^4\Pi$ and C $^4\Sigma^-$ upper state rovibronic energy levels and their associated quantum numbers. We also had a set of A–X, B–X and C–X frequencies for which the assigned quantum numbers had been verified through combination differences. Finally, Hopkins et al. (2009) measured some vibrational excited and overtone bands of the C–X transition. We use the model Hamiltonian fits and PGOPHER to produce empirical energy levels of these vibrationally excited C $^4\Sigma^-$ states. Table 3 details all the X $^4\Sigma^-$, A $^4\Pi$, B $^4\Pi$ and C $^4\Sigma^-$ spin-vibronic band energies which we include in the model refinement, while Table 5 details the transitions used.

The D $^4\Delta$ and A′ $^4\Phi$ energy levels are obtained indirectly using the A–X, D–A, D–A′ transitions. Given the difficulties in the model Hamiltonian parameters for the A $^4\Pi$ state, we decided to not use the energy levels from D $^4\Delta$ and A′ $^4\Phi$ model Hamiltonian parameters. Instead, we used the DUO energy levels for the A $^4\Pi$ state in combination with D–A transition frequencies to obtain combination differences for the D $^4\Delta$ state. After fitting to the D $^4\Delta$ state in DUO, we used the DUO D $^4\Delta$ state energies and the D–A′ transition frequencies to obtain combination differences for the A′ $^4\Phi$ state. We refine our model to both these D $^4\Delta$ and A′ $^4\Phi$ combination difference energies (see Table 4) and the D–A and D–A′ frequencies (see Table 6) that produced these combination differences.

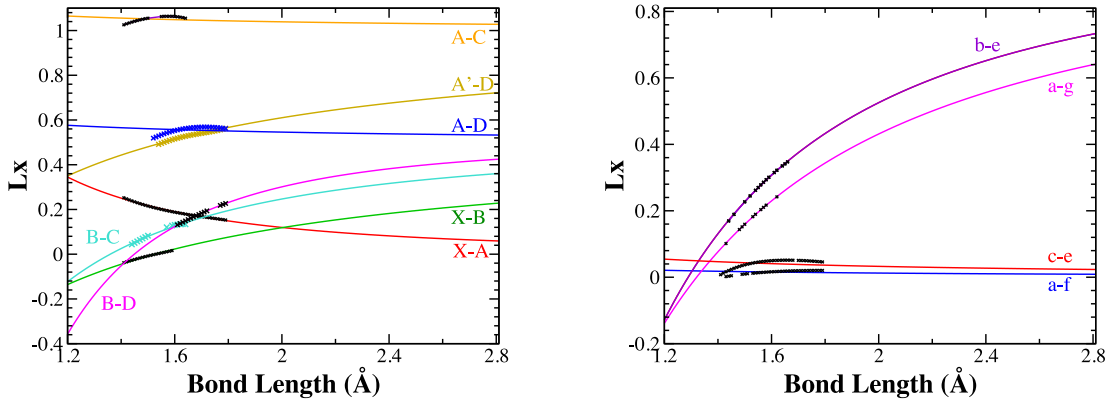

Figure 4. *Ab initio* off-diagonal Lx coupling matrix elements as calculated by McKemmish et al. (2016) in darker small crosses, and the fitted curves in lighter continuous curves.

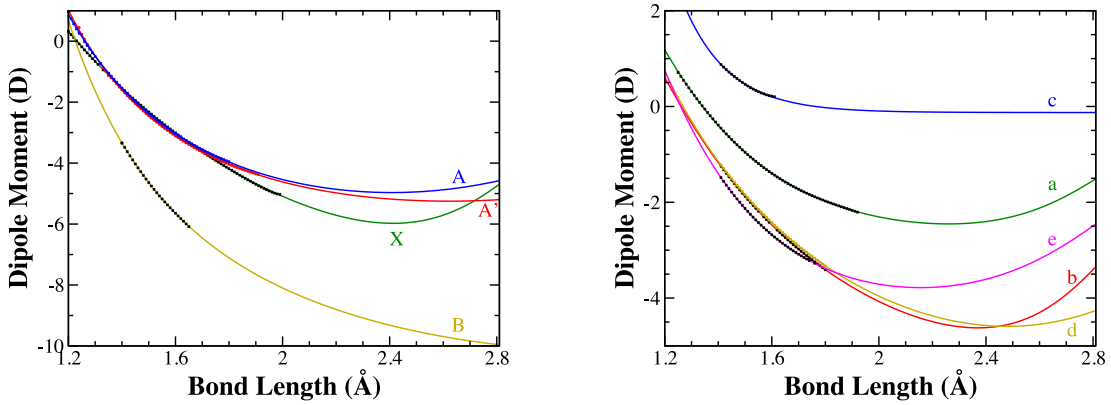

Figure 5. *Ab initio* diagonal diagonal dipole moment curves as calculated by McKemmish et al. (2016) in darker small crosses, and the fitted curves in lighter continuous curves.

For such a complex molecule, the refinement of the theoretical model to experimental data needs to be performed iteratively.

In the first step, we used the independent electronic state approximation to find PECs and diagonal spin–orbit couplings for each of the electronic states assuming that there was no interaction between electronic states. The independent state approximation was then relaxed through the inclusion of off-diagonal spin–orbit coupling and electronic angular momentum coupling terms.

The final parameters are detailed in the next section and provided in DUO input format as part of the supplementary information for this article.

2.3 Results

2.3.1 Potential energy curves

The PECs of the 13 electronic states is the most important component of the VO spectroscopic model. It controls the main rovibronic energy structure (i.e. the gaps between electronic states, the vibrational spacing and the rotational constants).

The high dissociation energy of VO means that the Morse oscillator is a good representation of the PECs for the low-lying electronic states of VO in the region of interest. This observation combined with the lack of reliable *ab initio* electronic structure results at long bond lengths/higher energies meant that we did not use *ab initio* PECs as input into DUO. Instead we directly used the EMO potential (Lee et al. 1999)

$$V(R) = T_e + D_e \times \left(1 - \exp\left[\left(\sum_{i=0}^{2} b_i \left(\frac{R^4 - R_e^4}{R^4 + R_e^4}\right)^i\right)(R - R_e)\right]\right)^2. \quad (1)$$

We started by setting the b_1 and b_2 parameters to zero, reducing the EMO to a simple Morse oscillator. We fixed the dissociation energy of the X $^4\Sigma^-$ state to 52 290 cm^{-1} based on experiment (Balducci, Gigli & Guido 1983); T_e+D_e for all other states was also fixed to this value, since all electronic states considered dissociate to the same atomic limit. Then the empirical excitation energies, harmonic frequencies and equilibrium bond lengths were used to find initial parameters. Note that in DUO default inverse length units, Å^{-1}, the Morse oscillator parameter $a = K\omega\sqrt{\mu/D_e}$ where if D_e and ω_e are in cm^{-1} and the reduced mass μ is in Dalton then $K = 0.121\,778\,815$. Where the term energies, harmonic frequencies and/or equilibrium bond lengths were unknown, we used *ab initio* electronic structure calculations data from Miliordos & Mavridis (2007) as summarized in Table 7.

The T_e, a and R_e parameters were then modified to reproduce the energy levels and frequencies in Tables 2–6. For the C $^4\Sigma^-$, D $^4\Delta$, f $^2\Pi$ and g $^2\Pi$ states, there was sufficient experimental data available to also optimize b_1 and b_2. The final parameters for the PEC of the spectroscopic model of VO are given in Table 1.

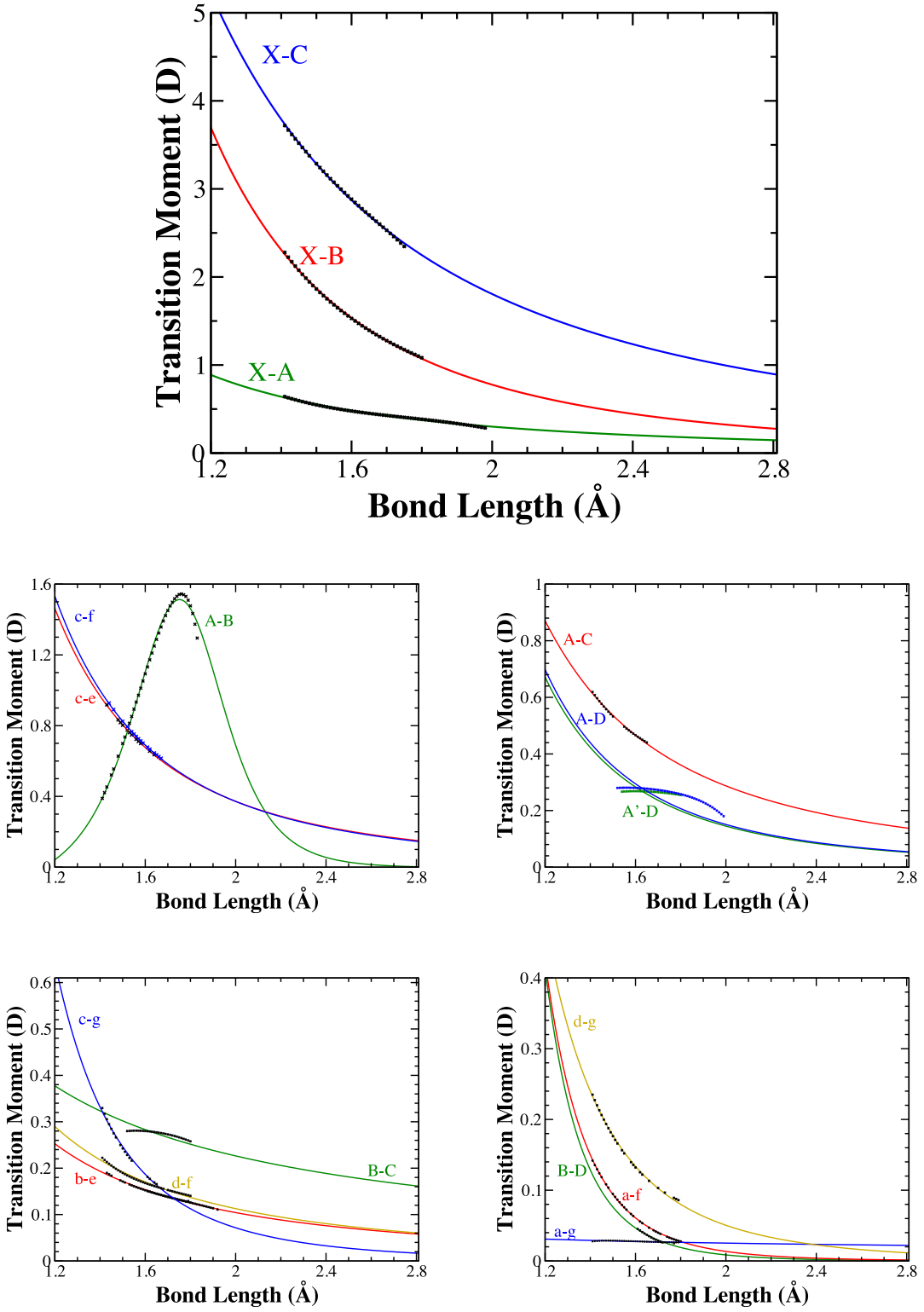

Figure 6. *Ab initio* off-diagonal diagonal dipole moment curves as calculated by McKemmish et al. (2016) in darker small crosses, and the fitted curves in lighter continuous curves.

2.3.2 *Spin–orbit coupling curves*

The spin–orbit coupling constants have two main effects in the spectroscopy of VO. First, diagonal coupling terms split the energies of the different spin components of the quartet or doublet electronic state with non-zero electronic angular momentum Λ. This significantly increases the complexity of the spectra of molecules with high spin states such as VO compared to more common main-group chemical molecules like H_2O. Secondly, off-diagonal

Table 2. Overview of empirical energy levels of the doublet states used to refine the spectroscopic model of VO, and quantification of the quality of this fit. MH indicates a Model Hamiltonian fit was used to evaluate the energy levels. RMS and Max are root-mean-squared-error and maximum deviations respectively against our VO spectroscopic model in cm^{-1}. 'No' gives the number of energy levels considered.

State	v''	Ω''	J'' range	No	RMS	Max
MH from Ram et al. (2002); Ram & Bernath (2005)						
$c\,^2\Delta$	0	1.5	4.5–39.5	72	0.272	0.423
		2.5	4.5–46.5	86	0.473	1.757
	1	1.5	4.5–39.5	72	1.078	3.295
$e\,^2\Phi$	0	2.5	6.5–39.5	68	0.109	0.117
		3.5	4.5–41.5	76	0.107	0.108
$f\,^2\Pi$	0	0.5	5.5–39.5	70	0.371	0.617
		1.5	4.5–46.5	86	0.100	0.227
	1	0.5	4.5–39.5	72	0.493	1.072
		1.5	4.5–33.5	60	0.948	1.007
	2	0.5	4.5–39.5	72	0.467	0.966
	3	0.5	6.5–35.5	59	0.572	0.976
$g\,^2\Pi$	0	0.5	0.5–19.5	40	0.192	0.376
		1.5	1.5–19.5	38	0.140	0.391
	1	0.5	0.5–19.5	39	0.271	0.541
	4	0.5	0.5–19.5	40	0.821	2.112
MH from Merer et al. (1987) using perturbations in B–X						
$d\,^2\Sigma^+$	2	0.5	0.5–39.5	82	1.079	8.534
	3	0.5	0.5–39.5	79	1.577	4.106

spin–orbit coupling causes mixing between different electronic states of both the same and different spins. This mixing gives intensity to spin- and symmetry-forbidden transitions, significantly increasing the complexity of the final spectra, though most of these new lines are quite weak compared to the allowed bands. In fact, the inclusion of off-diagonal spin–orbit coupling in our spectroscopic model is the major contributor (with L_x and L_y couplings playing a smaller but important role) to the very large number of transitions in the ExoMol VOMYT line list compared to the earlier Plez and Kurucz line lists.

We fit the absolute value of the *ab initio* data to the form:

$$\mathrm{SO}^{\mathrm{fit}} = \mathrm{SO}^{\mathrm{fit}}_{\infty}\left(1 + \frac{k}{R^m}\right) \tag{2}$$

where R is the bond distance, k, m are parameters, and $m \geq 1$ is used to ensure sufficiently fast convergence to the atomic value SO_∞. For many coupling elements, the data are insufficient to provide a strong constraint on the variable parameters and consequently there can be a lot of variance in the fitted value of $\mathrm{SO}^{\mathrm{fit}}_{\infty}$. Thus, different spin–orbit curves should be compared by the equilibrium value not the asymptotic value because the equilibrium value is generally interpolated not extrapolated.

To fit experimental data, and introduce the correct sign and phase information, we included a further multiplicative value, f, i.e.

$$\mathrm{SO}^{\mathrm{DUO}} = \mathrm{SO}^{\mathrm{DUO}}_{\infty}\left(1 + \frac{k}{R^m}\right) = f\,\mathrm{SO}^{\mathrm{fit}}_{\infty}\left(1 + \frac{k}{R^m}\right), \tag{3}$$

f may be complex.

The specifications for the diagonal spin–orbit coupling curves are tabulated in Table 8, while the *ab initio* data points and fits are plotted for quartets and doublets in Fig. 2. The specifications for the off-diagonal spin–orbit coupling curves are tabulated in Table 9, while the *ab initio* data points and fits are plotted in Fig. 3. One result worth commenting about is the $f\,^2\Pi$ and $g\,^2\Pi$ spin–orbit coupling. Experimentally, there is little evidence of coupling between the $f\,^2\Pi$ and $g\,^2\Pi$ states; the fact that our *ab initio* electronic

Table 3. Overview of the empirical energy levels of the $X\,^4\Sigma^-$, $A\,^4\Pi$, $B\,^4\Pi$ and $C\,^4\Sigma^-$ state used in fitting, and quantification of the quality of this fitting. MH stands for Model Hamiltonian and CD stands for Combination Differences. Also included are the RMS and Max deviations against VO spectroscopic model in cm^{-1}. The 'No' column gives the number of energy levels considered.

State	v''	Ω''	J'' range	No	RMS	Max
MH from Adam et al. (1995)						
$X\,^4\Sigma^-$	0	0.5	0.5–50.5	101	0.014	0.040
		1.5	1.5–50.5	100	0.015	0.041
	1	0.5	0.5–50.5	102	0.017	0.034
		1.5	1.5–50.5	100	0.028	0.051
CD from Cheung et al. (1982b)						
$A\,^4\Pi$	0	−0.5	13.5–63.5	96	0.494	1.989
		0.5	20.5–68.5	67	0.415	0.618
		1.5	20.5–49.5	35	0.228	0.302
		2.5	7.5–66.5	84	0.259	0.355
CD from Cheung et al. (1994); Adam et al. (1995)						
$B\,^4\Pi$	0	−0.5	5.5–47.5	80	0.972	1.402
		0.5	4.5–45.5	68	1.628	2.380
		1.5	7.5–40.5	51	0.505	1.242
		2.5	7.5–47.5	76	0.108	0.393
	1	−0.5	5.5–24.5	23	2.421	3.732
		0.5	10.5–35.5	27	1.220	1.830
		1.5	9.5–31.5	20	0.221	0.300
		2.5	7.5–33.5	43	0.213	0.404
CD from Cheung et al. (1982a)						
$C\,^4\Sigma^-$	0	0.5	0.5–41.5	53	0.062	0.3455
		1.5	1.5–38.5	60	0.260	1.9935
MH from Hopkins et al. (2009)						
$C\,^4\Sigma^-$	1	0.5	0.5–9.5	19	1.277	1.432
		1.5	1.5–9.5	18	1.425	1.570
	2	0.5	0.5–9.5	20	3.286	3.43
		1.5	1.5–9.5	18	2.937	2.964
	3	0.5	0.5–9.5	10	1.655	1.857
		1.5	1.5–9.5	9	1.872	2.040
	4	0.5	0.5–9.5	20	1.705	1.906
		1.5	1.5–9.5	18	1.873	2.093
	5	0.5	0.5–9.5	20	2.140	2.796
		1.5	1.5–9.5	18	2.007	2.480
	6	0.5	0.5–9.5	18	0.949	1.466
		1.5	1.5–9.5	18	0.998	1.203

Table 4. Overview of the empirical energy levels of the $D\,^4\Delta$ and $A'\,^4\Phi$ states used in fitting, and the RMS and Max deviations against VO spectroscopic model (in cm^{-1}). The 'No' column gives the number of energy levels considered.

State	v''	Ω''	J'' range	No	RMS	Max
CD from A fit and D–A in Merer et al. (1987)						
$D\,^4\Delta$	0	0.5	6.5–23.5	10	2.325	2.446
		1.5	8.5–25.5	34	0.186	0.468
		2.5	14.5–14.5	2	0.460	0.469
		3.5	6.5–24.5	32	0.441	0.484
CD from D fit and D–A′ in Merer et al. (1987)						
$A'\,^4\Phi$	0	1.5	5.5–6.5	2	17.448	17.506
		2.5	8.5–28.5	8	8.435	10.269
		3.5	8.5–47.5	21	1.498	2.588
		4.5	13.5–42.5	7	4.072	5.710
	1	2.5	15.5–18.5	2	2.023	4.246
		3.5	13.5–46.5	30	1.108	2.272
		4.5	19.5–31.5	7	3.641	5.106
	2	3.5	15.5–39.5	21	0.662	1.324
		4.5	19.5–39.5	20	1.583	2.746

Table 5. Overview of the experimental frequencies for the A $^4\Pi$–X $^4\Sigma^-$, B $^4\Pi$–X $^4\Sigma^-$ and C $^4\Sigma^-$–X $^4\Sigma^-$ transitions from Cheung et al. (1982a,b, 1994); Adam et al. (1995) used in fitting, and the RMS and Max deviations against VO spectroscopic model in cm^{-1}. The 'No' column gives the number of frequencies considered.

Transition	v''	Ω''	J'' range	v'	Ω'	J' range	No	RMS	Max
A $^4\Pi$–X $^4\Sigma^-$	0	−0.5	17.5–49.5	0	0.5	16.5–50.5	42	0.376	0.633
		0.5	30.5–63.5		1.5	31.5–63.5	25	0.510	0.662
		1.5	17.5–49.5		1.5	16.5–49.5	20	0.237	0.315
		2.5	28.5–62.5		0.5	29.5–63.5	27	0.183	0.414
		2.5	8.5–65.5		1.5	8.5–66.5	46	0.076	0.260
		−0.5	19.5–49.5	1	0.5	18.5–50.5	35	0.393	0.593
		−0.5	30.5–63.5		1.5	31.5–63.5	15	0.396	0.686
		1.5	17.5–49.5		1.5	16.5–49.5	20	0.228	0.318
		2.5	8.5–33.5		1.5	8.5–32.5	24	0.086	0.232
B $^4\Pi$–X $^4\Sigma^-$	0	−0.5	6.5–46.5	0	0.5	7.5–46.5	38	0.932	1.290
		0.5	4.5–46.5		1.5	4.5–46.5	96	0.970	1.412
		1.5	7.5–37.5		0.5	6.5–37.5	36	0.517	0.959
		1.5	6.5–40.5		1.5	5.5–39.5	47	0.463	1.227
		2.5	8.5–36.5		0.5	7.5–35.5	15	0.077	0.102
		2.5	6.5–47.5		1.5	5.5–47.5	105	0.107	0.226
	1	−0.5	5.5–23.5	0	1.5	5.5–23.5	21	2.429	3.442
		1.5	8.5–28.5		1.5	7.5–29.5	22	0.212	0.293
		2.5	6.5–33.5		1.5	5.5–33.5	60	0.220	0.429
C $^4\Sigma^-$–X $^4\Sigma^-$	0	0.5	4.5–40.5	0	0.5	4.5–40.5	44	0.041	0.138
		1.5	2.5–38.5		1.5	2.5–38.5	79	0.042	0.103

Table 6. Overview of the empirical DUO-derived frequencies for the D $^4\Delta$–A $^4\Pi$ and D $^4\Delta$–A′ $^4\Phi$ transitions from Merer et al. (1987) used in fitting, and the RMS and Max deviations against VO spectroscopic model in cm^{-1}. The 'No' column gives the number of frequencies considered.

Transition	v''	Ω''	J'' range	v'	Ω'	J' range	No	RMS	Max
D $^4\Delta$–A $^4\Pi$	0	0.5	6.5–23.5	0	−0.5	6.5–24.5	10	0.204	0.421
		1.5	8.5–24.5		0.5	7.5–25.5	47	0.309	0.682
		2.5	14.5–14.5		1.5	13.5–14.5	3	0.604	0.643
		3.5	6.5–24.5		2.5	5.5–23.5	41	0.442	0.500
D $^4\Delta$–A′ $^4\Phi$	0	0.5	2.5–7.5	0	1.5	3.5–6.5	6	11.201	11.266
		1.5	7.5–28.5		2.5	8.5–28.5	13	3.069	4.039
		2.5	7.5–48.5		3.5	8.5–47.5	49	0.922	1.877
		3.5	12.5–43.5		4.5	13.5–42.5	14	1.413	2.194
		1.5	14.5–18.5	1	2.5	15.5–18.5	4	0.588	0.636
		2.5	12.5–47.5		3.5	13.5–46.5	75	0.756	1.190
		3.5	18.5–31.5		4.5	19.5–31.5	14	7.292	8.219
	1	1.5	11.5–19.5	0	2.5	12.5–19.5	3	3.632	4.092
		2.5	13.5–39.5	2	3.5	14.5–39.5	53	0.785	1.018
		3.5	18.5–39.5		4.5	19.5–39.5	47	4.818	6.060

Table 7. Other data used to refine the spectroscopic model.

State	Method/Source	Property	Value
Experimental data			
A $^4\Pi$	Tentative assignment[1]	ω_e	884 cm^{-1}
a $^2\Sigma^-$	Low-res. Photoelectron[2]	T_e	5630 cm^{-1}
Ab initio data[3]			
a $^2\Sigma^-$	C-icMRCI+DKH2+Q/BP	r_e	1.582 Å
		ω_e	1020 cm^{-1}
b $^2\Gamma$	C-icMRCI+DKH2+Q/BP	T_e	8849 cm^{-1}
		r_e	1.577 Å
	icMRCI+Q/B	ω_e	1025 cm^{-1}
e $^2\Phi$	icMRCI+Q/B	ω_e	934 cm^{-1}
c $^2\Delta$	icMRCI/BP	SO	180 cm^{-1}

Notes. [1]Merer (1989), [2]Wu & Wang (1998), [3]Miliordos & Mavridis (2007).

Table 8. Diagonal spin–orbit coupling matrix elements in cm^{-1}. The 'Fit?' column provides information about the degree to which the *ab initio* results could be modelled by the functional form in equation (2): GF means good fit, OF means satisfactory fit with minor deviations, WC means the results showed the run concavity (i.e. not going towards an asymptote), TPS means there is a turning point in the *ab initio* data but the magnitude of the changes is very small – data are fit by constraining $k = 0$. Most *ab initio* results are from 1.41 to 1.80 Å; Fig. 2 provides the data points explicitly. The equilibrium spin–orbit matrix elements are evaluated at 1.58 Å for the b and c states, at 1.63 Å for the A′, e, f, g states, at 1.64 Å for the A and B states and at 1.69 Å for the D state. *f* refers to the multiplicative factor described in equation (3).

	Ab Initio		Extrapolation parameters				DUO fit			Exp
	$SO^{\text{ab initio}}_{R_{eq}}$	Fit?	SO^{fit}_{∞}	k	m	$SO^{fit}_{R_{eq}}$	f	$\lvert SO\rvert^{DUO}_{\infty}$	$\lvert SO\rvert^{DUO}_{R_{eq}}$	$\lvert SA\Lambda\rvert$
A′	256.26	OF	181.8	0.66	1*	255.16	0.987i	179.36	251.71	256.2
A	68.99	GF	140.3	−0.97	1.31	69.06	0.762i	106.98	52.64	52.8
B	90.63	GF	63.5	1.21	2.11	90.63	1.070i	67.98	97.02	96.9
D	169.81	WC	155.2	0.15	1*	169.28	0.849i	131.70	143.68	143.5
b	0.71	GF	2.1	−1.05	1*	0.72	1			
c	188.02	TPS	187.7	0*	N/A	187.73	0.958	179.81	179.81	$p^{\#}$
e	176.54	WC	140.5	0.41	1*	175.62	1.055i	148.28	185.34	$p^{\#} + 6.1$
f		Exp	126.4	0*	N/A	126.41	−i	126.41	126.41	$p^{\#} - 54.4$
g	61.96	OF	76.8	−1.47	4*	60.76	−0.949i	72.82	57.65	59.8

*Parameter constrained. #Experiment constrains the ratio between these three spin–orbit matrix elements, but not their exact value. Based on the theory calculations of Miliordos & Mavridis (2007), we constrained $p = 180\ cm^{-1}$.

structure calculations give a large spin–orbit coupling constant is indicative of mixing between the f $^2\Pi$ and g $^2\Pi$ in the *ab initio* calculation (since the two states share the same spin and symmetry). We choose to include this spin–orbit coupling because it should improve dipole moment matrix elements involving the f $^2\Pi$ and g $^2\Pi$ states. In most cases, *ab initio* spin–orbit coupling constants were found to be generally reliable; in particular, our diagonal spin–orbit constants were usually very accurate. However, calculations involving states A $^4\Pi$, B $^4\Pi$, f $^2\Pi$ or g $^2\Pi$ showed much larger errors. In particular the f $^2\Pi$, g $^2\Pi$ state were often not in the right order with respect to each other and the h $^2\Pi$ state. These errors partially arise due to significant mixing between nearby states of the same spin and symmetry: the A $^4\Pi$ and B $^4\Pi$ state share the same spin and symmetry and are only approximately 3000 cm^{-1} apart, while the f $^2\Pi$ and g $^2\Pi$ states are even closer at approximately 1000 cm^{-1} apart and within 3000 cm^{-1} of a third state of the same spin and symmetry, h $^2\Pi$. A specific example of the errors this caused in the final line list can be seen in the energy levels of the D state given in Table 10 with and without the inclusion of the D–g spin–orbit coupling constants (with other parameters optimized). The inclusion of the D $^4\Delta$–g $^2\Pi$ spin–orbit coupling constant significantly deteriorates the quality with which the DUO model reproduces the D $^4\Delta$ state combination differences. Given these *ab initio* difficulties combined with the fact there are other very closely lying $^2\Pi$ states that are not considered in our model, we choose not to include many diagonal spin–orbit coupling elements involving the f $^2\Pi$ and g $^2\Pi$ states. The only exceptions are the f $^2\Pi$–g $^2\Pi$ and A $^4\Pi$–g $^2\Pi$ spin–orbit coupling elements.

2.3.3 Lx *coupling*

The Lx coupling is the *x* component of the electronic angular momentum coupling between electronic states. It acts in a similar way to the spin–orbit coupling to give rise to mixing of electronic states and the weak occurrence of some previously forbidden spectral lines. However, Lx coupling has a much smaller effect because diagonal elements and coupling between electronic states of different spins is strictly zero.

We fit the absolute of the *ab initio* data to the form:

$$\mathrm{Lx}^{\mathrm{fit}} = \mathrm{Lx}^{\mathrm{fit}}_{\infty} + \frac{k}{R^m}, \tag{4}$$

where $m \geq 1$ to ensure sufficiently fast convergence to the atomic limiting value Lx_{∞}. When the data supports a particular logical rational value of Lx_{∞} (e.g. 0 or 1), this value is fixed.

The input to the DUO program was given by

$$\mathrm{Lx}^{\mathrm{DUO}} = f\mathrm{Lx}^{\mathrm{fit}}. \tag{5}$$

The parameter f was used to provide the correct sign and phase information appropriate to DUO and may be complex; getting the sign correct from MOLPRO output to DUO output is non-trivial (Patrascu et al. 2014). It could also be used in fitting; however, this was not done in the case of VO.

The *ab initio* points and the fit are shown graphically in Fig. 4. The specifications of the *ab initio* data, the fit and the DUO input are given in Table 11.

It is difficult to judge the accuracy of the theoretical electronic angular momentum terms. For VO, inclusion of all of these terms did not adversely affect the fit; therefore we included non-zero terms involving the lowest 13 electronic states. Note, however, that there are a significant number of electronic states just above 20 000 cm^{-1} that will couple to lower states, in particular the f $^2\Pi$, g $^2\Pi$, C $^4\Sigma^-$ and D $^4\Delta$ states.

2.3.4 *Spin–spin and spin–rotational constants*

Traditionally, the model Hamiltonians used to fit observed data often included empirical spin–spin and spin–rotation elements. These matrix elements always involve only one electronic state. They quantify how the energy of a particular energy level depends on its spin state and the rotational levels. The effect of the spin–spin coupling is much smaller than the spin–orbit coupling, but can be important for high accuracy and when there is no orbital angular momentum (and therefore no diagonal spin–orbit coupling). The spin–rotation element is again generally a small effect needed only for very high accuracy reproduction of energy levels. The spin–spin and spin–rotation elements are physical components of the total spin-rovibronic Hamiltonian (Tennyson

Table 9. Off-diagonal spin–orbit coupling matrix elements in cm^{-1} evaluated at $R = 1.59$ Å and $R \to \infty$. See the caption for Table 8 for the meanings of the abbreviations in the comments column. Most *ab initio* results are from 1.41 to 1.80 Å; Fig. 3 provides the data points explicitly. The matrix element specifies the Σ quantum number for which the coupling element is evaluated, with a negative sign on either electronic state indicating that the electronic angular momentum, L_z, expectation value for that electronic state is negative for the signs of the DUO wavefunction.

	Ab Initio		Extrapolation parameters					
	$\lvert SO\rvert^{\text{ab inito}}_{R=1.59}$	Fit?	$\lvert SO\rvert^{\text{fit}}_{\infty}$	k	m	$\lvert SO\rvert^{\text{fit}}_{R=1.59}$	f	Matrix element
X–A	65.98	GF	91.6	−0.45	1*	65.82	−1	$\langle -^3\Pi_x, 0.5\lvert\hat{H}_{SO}\rvert^3\Sigma^-, 1.5\rangle$
X–B	7.89	OF	86.1	−1.43	1*	8.70	−1	$\langle ^3\Pi_x, 0.5\lvert\hat{H}_{SO}\rvert^3\Sigma^-, 1.5\rangle$
A′–D	43.03	OF	41.5	1.31	7.70	43.06	i	$\langle ^3\Phi_x, 1.5\lvert\hat{H}_{SO}\rvert^3\Delta_y, 0.5\rangle$
A–B	2.70	TPS	2.2	0*	N/A	2.22	i	$\langle -^3\Pi_x, 1.5\lvert\hat{H}_{SO}\rvert^3\Pi_y, 1.5\rangle$
A–C	6.39	WC	54.6	−1.41	1*	6.29	1	$\langle -^3\Pi_x, 0.5\lvert\hat{H}_{SO}\rvert^3\Sigma^-, 1.5\rangle$
A–D	45.37	WC	20.5	1.90	1*	44.89	−i	$\langle -^3\Pi_x, 0.5\lvert\hat{H}_{SO}\rvert^3\Delta_y, 1.5\rangle$
B–C	$41.70^{R=1.57}$	TPS	41.8	0.0	N/A	41.83	0	$\langle ^3\Pi_x, 0.5\lvert\hat{H}_{SO}\rvert^3\Sigma^-, 1.5\rangle$
B–D	4.73	OF	39.4	−1.38	1*	5.32	i	$\langle ^3\Pi_x, 0.5\lvert\hat{H}_{SO}\rvert^3\Delta_y, 1.5\rangle$
X–d	265.95	OF	277.6	−0.29	4*	265.19	−i	$\langle ^1\Sigma^+, -0.5\lvert\hat{H}_{SO}\rvert^3\Sigma^-, 0.5\rangle$
X–f	57.79	OF	60.6	−0.29	4*	57.88	0	$\langle -^1\Pi_x, 0.5\lvert\hat{H}_{SO}\rvert^3\Sigma^-, 1.5\rangle$
X–g	78.27	WC	89.4	−0.20	1*	78.40	0	$\langle -^1\Pi_x, 0.5\lvert\hat{H}_{SO}\rvert^3\Sigma^-, 1.5\rangle$
A′–b	82.28	TPS	82.0	0*	N/A	81.96	i	$\langle ^3\Phi_x, 1.5\lvert\hat{H}_{SO}\rvert^1\Gamma_y, 0.5\rangle$
A′–c	32.39	GF	140.6	−1.20	1*	32.35	i	$\langle ^3\Phi_x, 1.5\lvert\hat{H}_{SO}\rvert - ^1\Delta_y, 0.5\rangle$
A′–e	122.27	WC	80.1	0.83	1*	121.75	−i	$\langle ^3\Phi_x, 0.5\lvert\hat{H}_{SO}\rvert^3\Phi_y, 0.5\rangle$
A–a	48.76	TPS	48.5	0*	N/A	48.48	−1	$\langle ^1\Sigma^-, -0.5\lvert\hat{H}_{SO}\rvert - ^3\Pi_y, 1.5\rangle$
A–c	8.89	TPS	8.6	0*	N/A	8.63	i	$\langle -^1\Delta_x, 0.5\lvert\hat{H}_{SO}\rvert - ^3\Pi_y, 1.5\rangle$
A–d	62.02	WC	10.6	7.58	1*	60.92	1	$\langle ^1\Sigma^+, -0.5\lvert\hat{H}_{SO}\rvert - ^3\Pi_y, 1.5\rangle$
A–f	22.33	TPS	25.0	0*	N/A	25.01	0	$\langle -^3\Pi_x, 0.5\lvert\hat{H}_{SO}\rvert - ^1\Pi_y, 0.5\rangle$
A–g	216.32	WC	171.5	0.40	1*	215.13	1	$\langle -^3\Pi_x, 0.5\lvert\hat{H}_{SO}\rvert - ^1\Pi_y, 0.5\rangle$
B–a	16.37	GF	48.8	−2.72	3.05	16.45	1	$\langle ^3\Pi_x, 1.5\lvert\hat{H}_{SO}\rvert^1\Sigma^-, 0.5\rangle$
B–c	8.89	TPS	8.6	0*	N/A	8.63	−i	$\langle -^1\Delta_x, 0.5\lvert\hat{H}_{SO}\rvert^3\Pi_y, 1.5\rangle$
B–d	6.96	GF	13.8	−1.80	2.79	6.98	−2.17i	$\langle ^1\Sigma^+, 0.5\lvert\hat{H}_{SO}\rvert^3\Pi_y, 1.5\rangle$
B–f	$12.14^{R=1.65}$	WC	−20.8	−2.49	1*	11.82	0	$\langle ^3\Pi_x, 0.5\lvert\hat{H}_{SO}\rvert - ^1\Pi_y, 0.5\rangle$
B–g	$12.86^{R=1.47}$	WC	25.9	−0.74	1*	13.85	0	$\langle ^3\Pi_x, 0.5\lvert\hat{H}_{SO}\rvert - ^1\Pi_y, 0.5\rangle$
C–d	18.85	GF	77.2	−1.19	1*	19.22	−i	$\langle ^3\Sigma^-, 0.5\lvert\hat{H}_{SO}\rvert^1\Sigma^+, 0.5\rangle$
C–f	$6.40^{R=1.61}$	OF	17.4	−4.11	4*	6.20	0	$\langle -^1\Pi_x, 0.5\lvert\hat{H}_{SO}\rvert^3\Sigma^-, 1.5\rangle$
C–g	Not calculated		0*	0*	N/A		0	
D–c	$14.53^{R=1.58}$	OF	102.3	−1.34	1*	15.78	i	$\langle ^3\Delta_x, 0.5\lvert\hat{H}_{SO}\rvert - ^1\Delta_y, 0.5\rangle$
D–e	32.21	WC	35.2	−0.13	1*	32.26	−i	$\langle ^3\Delta_x, 1.5\lvert\hat{H}_{SO}\rvert^1\Phi_y, 0.5\rangle$
D–f	36.49	TPS	36.0	0*	N/A	36.04	0	$\langle ^3\Delta_x, 1.5\lvert\hat{H}_{SO}\rvert - ^1\Pi_y, 0.5\rangle$
D–g	34.53	GF	23.1	3.62	4.32	34.41	0	$\langle ^3\Delta_x, 1.5\lvert\hat{H}_{SO}\rvert - ^1\Pi_y, 0.5\rangle$
a–d	192.33	OF	200.7	−0.28	4*	191.80	i	$\langle ^1\Sigma^-, 0.5\lvert\hat{H}_{SO}\rvert^1\Sigma^+, 0.5\rangle$
a–f	78.62	GF	94.9	−0.27	1*	78.64	0	$\langle ^1\Sigma^-, -0.5\lvert\hat{H}_{SO}\rvert - ^1\Pi_y, 0.5\rangle$
a–g	68.86	OF	94.9	−0.27	1*	68.55	0	$\langle ^1\Sigma^-, -0.5\lvert\hat{H}_{SO}\rvert - ^1\Pi_y, 0.5\rangle$
b–e	69.01	TPS	68.8	0*	N/A	68.47	−i	$\langle -^1\Gamma_x, -0.5\lvert\hat{H}_{SO}\rvert^1\Phi_y, 0.5\rangle$
c–e	12.35	OF	76.4	−1.32	1*	13.21	−i	$\langle -^1\Delta_x, -0.5\lvert\hat{H}_{SO}\rvert^1\Phi_y, 0.5\rangle$
c_- f	19.21	OF	60.3	−1.09	1*	19.14	0	$\langle -^1\Delta_x, -0.5\lvert\hat{H}_{SO}\rvert - ^1\Pi_y, 0.5\rangle$
c–g	$34.66^{R=1.61}$	OF	134.4	−1.20	1*	33.36	0	$\langle -^1\Delta_x, -0.5\lvert\hat{H}_{SO}\rvert - ^1\Pi_y, 0.5\rangle$
d–f	53.52	WC	21.7	2.30	1*	52.99	0	$\langle ^1\Sigma^+, -0.5\lvert\hat{H}_{SO}\rvert - ^1\Pi_y, 0.5\rangle$
d–g	2.97	TPS	2.7	0*	N/A	2.67	0	$\langle ^1\Sigma^+, -0.5\lvert\hat{H}_{SO}\rvert - ^1\Pi_y, 0.5\rangle$
f–g	$150.95^{R=1.56}$	GF	111.86	0.54	1*	150.19	i	$\langle -^1\Pi_x, -0.5\lvert\hat{H}_{SO}\rvert - ^1\Pi_y, 0.5\rangle$

*Parameter constrained.

Table 10. Comparison of quality of the fit for D $^4\Delta$ state energy levels with and without the inclusion of the D $^4\Delta$–g $^2\Pi$ spin–orbit coupling constants.

				With D–g SO		No D–g SO	
State	Ω	J Range	No.	RMS (cm^{-1})	Max (cm^{-1})	RMS (cm^{-1})	Max (cm^{-1})
D $^4\Delta$	0.5	6.5–23.5	10	15.95	18.00	1.11	2.02
	1.5	8.5–25.5	35	7.43	10.24	0.65	1.33
	2.5	14.5–14.5	2	0.42	0.42	0.35	0.36
	3.5	6.5 –24.5	32	0.56	1.00	0.56	1.00

et al. 2016a). Though it is theoretically possible to calculate these terms, this is not routinely done due to computational difficulty and also because these terms are usually also empirical corrections for interactions that have been neglected in the model.

Since these are empirical terms that asymptotically go to zero, we decided to use the Surkus-polynomial expansion (Šurkus, Rakauskas & Bolotin 1984) formula for their matrix elements:

$$F(R) = \left(1 - \left(\frac{R^p - R_e^p}{R^p + R_e^p}\right)\right)\alpha, \quad (6)$$

Table 11. Off-diagonal Lx coupling constants evaluated at $R = 1.59$ Å and $R \to \infty$. See the caption for Table 9 for the meanings of the abbreviations in the comments column. Most *ab initio* results are from 1.41 to 1.80 Å; Fig. 4 provides the data points explicitly. In cases of TPS, we fit to the data based on the nearest logical Lx_∞.

	Ab Initio		Extrapolation parameters				
	$\lvert\mathrm{Lx}\rvert^{\text{ab inito}}_{R=1.59}$	Fit?	$\lvert\mathrm{Lx}\rvert^{\text{fit}}_{\infty}$	k	m	$\lvert\mathrm{Lx}\rvert^{\text{fit}}_{R=1.59}$	f
X–A	1.320	GF	1.5*	1.34	4.34	1.321	−1
X–B	0.016	GF	0.5*	−0.76	1*	0.020	−1
A′–D	0.512	OF	1*	−0.78	1*	0.510	+i
A–C	1.063	TPS	1*	0.08	1*	1.049	+1
A–D	0.549	TPS	0.5*	−0.72	4*	0.557	−i
B_- C	0.128	OF	0.5*	−0.86	1.76	0.121	−1
B–D	$0.131^{R=1.61}$	GF	0.5*	−1.44	2.86	0.117	+i
a–f	0.301	OF	1*	−1.54	1.70	0.300	−1
a–g	0.072	TPS	0*	0.10	1*	0.064	−1
b–e	0.016	TPS	0*	0.03	1*	0.016	−i
c–e	$0.217^{R=1.58}$	GF	1*	−1.46	1.36	0.223	−i
c–f	0.301	GF	1*	−1.54	1.70	0.300	+i
c–g	$0.175^{R=1.61}$	OF	1*	−1.32	1*	0.172	−i
d–f	0.049	TPS	0*	0.07	1*	0.041	−i
d–g	1.538	GF	2*	−1.12	1.93	1.542	−i

Note. *Parameter constrained.

Table 12. Spin–spin and spin–rotational constants, both experimental and fitted, in cm^{-1}. Good agreement is not expected in many cases as the experimental constants also account for other effects (see the text).

State		Fitted*	Exp
$\mathrm{X}\,^4\Sigma^-$	λ_{SS}	0.0529	2.0300
	γ_{SR}	0.0191	0.0225
$\mathrm{A}'\,^4\Phi$	λ_{SS}	−0.6030	
	γ_{SR}	0.4400	
$\mathrm{A}\,^4\Pi$	λ_{SS}	1.0410	1.8670
	γ_{SR}	0.0065	0.0038
$\mathrm{B}\,^4\Pi$	λ_{SS}	2.5869	2.6579
	γ_{SR}	0.0452	0.0336
$\mathrm{C}\,^4\Sigma^-$	λ_{SS}	0.8037	0.7469
	γ_{SR}	−0.0155	−0.0184
$\mathrm{D}\,^4\Delta$	λ_{SS}	0.2625	
	γ_{SR}	0.0160	
$\mathrm{c}\,^2\Delta$	γ_{SR}	0.2340	
$\mathrm{e}\,^2\Phi$	γ_{SR}	−0.0864	
$\mathrm{f}\,^2\Pi$	γ_{SR}	−0.1520	
$\mathrm{g}\,^2\Pi$	γ_{SR}	1.2500	

*Note that DUO actually takes as input $\frac{2}{3}\lambda_{SS}$; λ_{SS} values are tabulated to match experiment.

where $R_e = 1.6$ Å, $p = 2$ and α is an adjustable parameter, given by λ_{SS} for spin–spin constants and γ_{SR} for spin–rotation constants. Note that the form of this expression is such that the matrix elements go to zero asymptotically. The value of the included spin–spin and spin–rotation terms are specified in Table 12, and compared against previously empirical (equilibrium) values where available. In many cases, the previous empirical values agree quite well to our values. The major difference is the spin–spin constant of the $\mathrm{X}\,^4\Sigma^-$ state which is only about 2.5 per cent of the experimental value. This reduction occurs because the spin–orbit couplings (particularly between the X–d states) produce the same type of perturbation to the $\mathrm{X}\,^4\Sigma^-$ state energy levels as the spin–spin coupling constant. However, the effect on other energy levels will be different, and some spin–forbidden transitions may be given intensity through this mechanism. The importance of the X–d spin–orbit coupling explaining the splitting of the $\mathrm{X}\,^4\Sigma^-$ state energy levels could not be predicted by experiment, as the $\mathrm{X}\,^4\Sigma^-$ and $\mathrm{d}\,^2\Sigma^+$ states are more than 10 000 cm^{-1} apart; it is only the very large magnitude (approximately 250 cm^{-1}) of the spin–orbit coupling constant that makes this element important. This example illustrates that the spin–spin coupling constants are sometimes used as empirical corrections rather than a fundamental characteristic. Proper accounting for important spin–orbit coupling can provide a more accurate picture of the molecule's spectroscopy. Unfortunately, for higher lying electronic states, this is currently impossible for transition metal diatomics with the high density of electronic states and the quality of modern *ab initio* calculations (Tennyson et al. 2016a).

2.3.5 *Diagonal dipole moment curves*

All diagonal dipole moment curves use icMRCI/aug-cc-pVQZ wavefunctions, evaluated using finite-field methodology (McKemmish et al. 2016). As previously discussed, there were significant convergence difficulties at long bond lengths. We thus choose to use *ab initio* points only where the calculations were trusted and the dipole moment curves smooth; this range is given in Table 13. Fortunately, the most physically important bond lengths were generally stable. However, we needed smooth, physically reasonable dipole moment curves to the boundary of the DUO grid to avoid adding spurious peaks to the spectrum (which can occur when the dipole moment curves or its derivatives have discontinuities). Physically, at long bond lengths, the dipole moment goes to zero when the system dissociates to neutral species; the unknown is how quickly this process occurs and the form of the intermediate dipole moment curve.

We choose to fit to a newly developed functional form of the dipole moment curve near a long bond length neutral/ionic crossing. This form will be fully derived, justified and possibly refined in a future theoretical paper, but is sufficiently accurate for current purposes. In basic terms, the model involves two diabatic states, the ionic and covalent, that interact to form an avoided crossing. The two diabatic states mix to form an adiabatic ground state which is ionic at short bond lengths, covalent at long bond lengths and has mixed character near the avoided crossing (note there is also an

Table 13. Diagonal dipole moment in DUO, where dipole moment is given in Debye. The equilibrium dipole moment for the a, b, c and d states is evaluated at 1.58 Å, at 1.63 Å for the A′ and e states, at 1.64 Å for the A and B states and at 1.59 Å for the X state.

State	*Ab Initio*		Extrapolation parameters					Fit characteristics			
	Range (Å)	$\mu_{R_{eq}}^{ab\ initio}$	j	m	t	l_1	l_2	$\mu_{R_{eq}}^{fit}$	$\mu'^{fit}_{R_{eq}}$	$\lvert\mu\rvert^{fit}_{max}$	R for $\lvert\mu\rvert^{fit}_{max}$
X $^4\Sigma^-$	1.15–1.99	−2.943	3*	−13.440	3.830	0.000	−8.812	−2.958	−6.656	−5.975	2.413
A′ $^4\Phi$	1.24–1.91	−3.281	3.493	−2.801	2.503	13.519	−28.013	−3.279	−5.401	−4.623	2.370
A $^4\Pi$	1.20–1.80	−3.263	2.617	−4.356	2.320	11.368	−23.962	−3.253	−5.302	−4.967	2.408
B $^4\Pi$	1.40–1.65	−5.996	3*	−0.846	6.123	18.798	−42.106	−5.993	−8.209	−10.171	3.237
a $^2\Sigma^-$	1.25–1.92	−1.319	0.859	−5.042	0.630	6.478	−13.689	−1.311	−4.008	−2.453	2.259
b $^2\Gamma$	1.41–1.80	−2.359	1.876	−9.668	2.468	3.058	−11.127	−2.361	−5.673	−4.623	2.37
c $^2\Delta$	1.41–1.61	0.244	Fit to 32 298.656 exp [−7.443R]					0.252	−1.878		
d $^2\Sigma^+$	1.41–1.80	−2.318	1.368	−2.849	2.819	4.671	−14.822	−2.315	−5.520	−4.590	2.479
e $^2\Phi$	1.41–1.76	−2.814	1.039	−4.333	0.719	12.126	−21.054	−2.857	−4.189	−3.782	2.155

*Constrained to ensure reasonable fit.

adiabatic excited state with the opposite characteristics that is not considered here). The dipole moment curve of this adiabatic ground state depends on the contribution of the ionic state and the dipole moment of the ionic state; this yields the functional form:

$$\mu_{GS}(R) = \frac{\left(\sqrt{4j^2+\lambda^2(R)}+\lambda(R)\right)^2 \mu_{Ionic}(R)}{\left(\sqrt{4j^2+\lambda(R)^2}+\lambda(R)\right)^2+4j^2}. \quad (7)$$

The μ_{ionic} is a functional form of the dipole moment of the ionic diabatic state, empirically expanded.

$$\mu_{ionic}(R) = tR + l_1R^{-1} + l_2R^{-3}. \quad (8)$$

Note that the second and third terms are found empirically to be necessary for a good fit, indicating the ionic state is not quite a true diabatic state in the traditional definition. Nevertheless, the use of pseudo-diabatic representation is useful. The j parameter controls the interaction between the ionic and covalent diabatic potentials and therefore how sharp the transition is. The $\lambda(R)$ function controls the distance between the two diabatic states and their crossing points and is of the form $\lambda(R) = m(R-d)(R-k)$, where k and d are the crossing points of the ionic and covalent diabatic curves (assuming that the ionic curve is a quadratic function of energy and the covalent curve is a linear or constant function) and m together with j controls the depth of the ionic well. We constrain k = 2.75 Å; this is the predicted location of the avoided crossing of the X $^4\Sigma^-$ state (Miliordos & Mavridis 2007). Physically, d is approximately the short bond length where the energy of the harmonic potential of the ionic state equals the energy of the covalent state (which is to a first approximation the dissociation energy); this was constrained to d = 1 Å without significantly affecting the quality of the fit.

The *ab initio* points and final fitted curves are shown graphically in Fig. 5, with quantitative data in Table 13.

The f $^2\Pi$, C $^4\Sigma^-$, g $^2\Pi$ and D $^4\Delta$ diagonal dipole moments are not needed because the T_e of these states are above 16 000 cm^{-1} and thus their thermal population is negligible at the temperatures considered for this line list.

2.3.6 *Off-diagonal dipole moments*

Off-diagonal dipole moment curves were generally well fitted by the form:

$$\mu_{OD} = \frac{k}{R^m}. \quad (9)$$

Table 14. Off-diagonal dipole moments in DUO; values are given in Debye.

	Ab Initio	Extrapolation parameters		
	$\lvert\mu\rvert^{ab\ initio}_{R=1.59}$	k	m	$\lvert\mu\rvert^{fit}_{R=1.59}$
X–A	0.19	1.306	2.122	0.192
X–B	0.613	6.451	3.054	0.616
X–C	1.149	7.627	2.079	1.145
A′–D	0.106	1.195	3*	0.112
A–B	0.067	Inbuilt DUO interpolation		
A–C	0.186	1.294	2.172	0.186
A–D	0.11	0.452	1*	0.11
B–C	0.06	0.480	2.428	0.061
B–D	$0.018^{R=1.61}$	1.657	7.596	0.019
a–f	0.025	1.454	6.75	0.025
a–g	0.011	0.033	0.397	0.011
b–e	0.061	0.346	1.733	0.061
c–e	$0.275^{R=1.58}$	2.384	2.68	0.27
c–f	0.276	2.539	2.772	0.276
c–g	$0.071^{R=1.61}$	1.408	4.299	0.076
d–f	0.067	0.407	1.848	0.068
d–g	0.052	1.045	4.371	0.054

*Parameter constrained.

However, for some cases, generally involving higher electronic states, this fit was not good. For the A–B dipole moment where very atypical behaviour with bond length was observed (probably due to state mixing), we put the *ab initio* points into DUO and then used the inbuilt interpolation routine. For other results, we determined that the quality of the *ab initio* calculations were not sufficiently reliable to trust the non-typical behaviour; however, the magnitude of the transition moment is probably reasonably reliable (and in any case, there is no other source of data). In these cases, we fixed m and fit k to the available data.

All results are tabulated in Table 14 and shown graphically in Fig. 6.

The f–g transition moment is not included in the calculation because the T_e of the f $^2\Pi$ state is above 16 000 cm^{-1} and thus its thermal population is negligible even at 5000 K.

2.3.7 *Summary of spectroscopic model*

Our DUO model for VO includes the following coupling terms:

(i) 13 PECs
(ii) four diagonal quartet spin–orbit coupling curves
(iii) five diagonal doublet spin–orbit coupling curves
(iv) five off-diagonal quartet–quartet spin–orbit coupling curves

(v) four off-diagonal doublet–doublet spin–orbit coupling curves
(vi) 15 off-diagonal quartet–doublet spin–orbit coupling curves
(vii) seven off-diagonal quartet–quartet electronic angular momentum coupling curves
(viii) eight off-diagonal doublet–doublet electronic angular momentum coupling curves
(ix) six diagonal quartet spin–spin coupling curves
(x) six diagonal quartet spin–rotation coupling curves
(xi) three diagonal doublet spin–rotation coupling curves
(xii) two diagonal lambda doubling curves
(xiii) nine diagonal dipole moment curves
(xiv) nine quartet off-diagonal dipole moment curves and
(xv) eight doublet off-diagonal dipole moment curves.

This is the most sophisticated DUO spectroscopic model of a diatomic system produced so far. The model, as specified by input to DUO, is given in the supplementary data.

2.4 Assessing quality of spectroscopic model against experimental energies

For the X state, we were able to accurately reproduce the empirical energy levels. This is evidenced by the relatively low obs-calc residuals (less than 0.05 cm^{-1} in all cases) for the X state shown in Table 3.

For higher lying electronic states, however, the choice and magnitude of spin–orbit and electronic angular momentum terms were not supported by as much experimental evidence. This is partially because there are many couplings to higher electronic states not considered in the DUO model for VO.

Quartet states have four spin–orbit components that couple differently to other electronic states to produce very distinctive splitting between the components. Nevertheless, sub cm^{-1} accuracy in the fits for the quartet states was generally achieved, as shown in Tables 3–6. In examining these tables, it is important to note that the optimisation did not weight all empirical data equally. The highest weights were put on the A $^4\Pi$, B $^4\Pi$ and C $^4\Sigma^-$ transitions confirmed by combination difference. The associated combination difference energies were attributed a higher weight than the PGOPHER energy levels. This accounts for the larger errors in the higher vibrational levels of the C $^4\Sigma^-$ state compared to energies associated with the C $^4\Sigma^-$ state ground vibrational levels. Furthermore, the D $^4\Delta$ and A′ $^4\Phi$ energy levels were optimized significantly less than the X $^4\Sigma^-$, A $^4\Pi$, B $^4\Pi$ and C $^4\Sigma^-$ energy levels as the former do not contribute to the primary absorption bands of VO; thus errors in their positions will not significantly affect the utility of the line list. This accounts for the larger errors in the A′ $^4\Phi$ state compared to the other quartets, particularly for those spin-rovibronic bands for which very few lines are assigned.

For the c $^2\Delta$, e $^2\Phi$, f $^2\Pi$ and g $^2\Pi$ doublets, as demonstrated by Table 2, a very good fit could usually be obtained because there was only one spin–orbit interval to reproduce; the biggest difficulties occurred with high vibrational states of f $^2\Pi$ and g $^2\Pi$. Though more sophisticated PECs might reduce these errors, we believe that they probably originate from inadequate treatment of spin–orbit coupling, particularly with respect to electronic states not considered in our spectroscopic models. We thus chose to use a smaller number of parameters.

The d $^2\Sigma^+$ state parameters were optimized predominantly to the frequencies and energies of the B $^4\Pi$ state, as this was the experimental origin of the PGOPHER model Hamiltonian parameters. This accounts for the larger errors in this state.

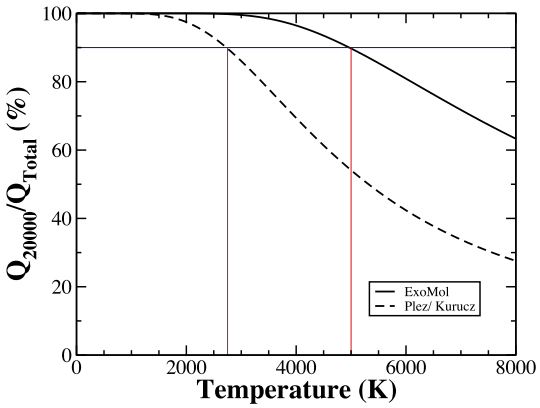

Figure 7. Ratio of effective partition function used in the VO line list, $Q_{20\,000}$, to the converged total value, Q_{total}. This ratio gives a measure of completeness of the VO line list as a function of temperature.

3 THE LINE LIST

3.1 Methodology

Direct solution of the nuclear-motion Schrödinger equation for diatomics systems with many coupled electronic states, and a variety of spins and symmetries has recently been made possible by the development of the program DUO (Yurchenko et al. 2016b). DUO has previously been used to model three electronic states for AlO by Patrascu et al. (2014), who computed a line list using this model (Patrascu, Tennyson & Yurchenko 2015). Lodi, Yurchenko & Tennyson (2015) consider six coupled electronic states in their study on ScH and Yurchenko et al. (2016a) constructed a line list for CaO using five electronic states. This is the first example where such a large number (13) of states have been considered. The above references give full details of the underlying theory used here to solve the rovibronic problem. All VO calculations were made without modification to the main DUO code base. As time considerations for diatomic molecules are minimal, for our final line list we used 301 grid points between 1.2 and 4.0 Å in these calculations.

The lower energy threshold was set to 20 000 cm^{-1}. This means our line list is 90 per cent complete at 5000 K, as shown in Fig. 7.

However, dipole moments were not included for transitions that originated in the C $^4\Sigma^-$, f $^2\Pi$ and g $^2\Pi$ states (i.e. states with T_e above 16 000 cm^{-1}) because these would be negligible given the very small population in these electronic states even at 5000 K.

The upper energy threshold was set at 50 000 cm^{-1}, just below the dissociation energy at 52 290 cm^{-1} (Balducci et al. 1983). The frequency range considered is up to 35 000 cm^{-1}; however, the line list will not fully describe emission spectroscopy of high lying energy levels due to the lower energy threshold.

At this stage, we have produced a DUO VO line list from the VOMYT spectroscopic model (and it is these energies and frequencies that are used in the comparisons in Tables 4–8). To increase the line list's accuracy, we will make one final modification. 781 DUO energies were substituted with the A $^4\Pi$, B $^4\Pi$ and C $^4\Sigma^-$ experimental energies derived from combination differences as specified above to form the final VOMYT line list.

3.2 Results

A line list, known as VOMYT, was calculated for $^{51}V^{16}O$ which contains 277 million transitions. For compactness and ease of use, it is divided into separate energy level and transition files. This is done

Table 15. Extract from the *.states file for $^{51}V^{16}O$.

1 n	2 $\tilde{E}$	3 g	4 J	5 τ	6 $+/-$	7 e/f	8 State	9 v	10 Λ	11 Σ	12 Ω
1453	19 124.638 77	32	1.5	1.03E−07	+	f	C4Sigma−	2	0	0.5	0.5
1454	19 199.409 66	32	1.5	1.77E−04	+	f	d2Sigma+	9	0	0.5	0.5
1455	19 219.561 57	32	1.5	6.42E−03	+	f	Ap4Phi	14	3	−1.5	1.5
1456	19 363.888 32	32	1.5	1.96E−05	+	f	A4Pi	12	1	−1.5	−0.5
1457	19 397.778 72	32	1.5	1.88E−05	+	f	A4Pi	12	1	−0.5	0.5
1458	19 430.929 90	32	1.5	1.81E−05	+	f	A4Pi	12	1	0.5	1.5
1459	19 444.433 27	32	1.5	7.31E−07	+	f	B4Pi	8	1	−1.5	−0.5
1460	19 499.138 05	32	1.5	7.21E−07	+	f	B4Pi	8	1	−0.5	0.5
1461	19 561.623 06	32	1.5	7.11E−07	+	f	B4Pi	8	1	0.5	1.5
1462	19 627.442 67	32	1.5	5.70E−04	+	f	a2Sigma−	15	0	0.5	0.5
1463	19 695.129 98	32	1.5	1.59E−05	+	f	f2Pi	3	1	−0.5	0.5
1464	19 782.220 31	32	1.5	3.21E−03	+	f	X4Sigma−	22	0	0.5	0.5
1465	19 788.599 04	32	1.5	3.21E−03	+	f	X4Sigma−	22	0	1.5	1.5
1466	19 844.136 79	32	1.5	2.13E−05	+	f	D4Delta	1	2	−1.5	0.5
1467	19 899.602 78	32	1.5	1.28E−04	+	f	g2Pi	2	1	−0.5	0.5
1468	19 939.215 99	32	1.5	2.13E−05	+	f	D4Delta	1	2	−0.5	1.5
1469	19 944.050 45	32	1.5	1.87E−05	+	f	f2Pi	3	1	0.5	1.5
1470	19 952.355 83	32	1.5	1.02E−07	+	f	C4Sigma−	3	0	1.5	1.5
1471	19 955.483 62	32	1.5	1.02E−07	+	f	C4Sigma−	3	0	0.5	0.5
1472	19 964.052 28	32	1.5	3.68E−03	+	f	c2Delta	11	2	−0.5	1.5
1473	20 017.119 81	32	1.5	NaN	+	f	g2Pi	2	1	0.5	1.5
1474	20 017.380 50	32	1.5	NaN	+	f	Ap4Phi	15	3	−1.5	1.5
1475	20 096.782 21	32	1.5	NaN	+	f	d2Sigma+	10	0	0.5	0.5
1476	20 140.401 62	32	1.5	NaN	+	f	A4Pi	13	1	−1.5	−0.5
1477	20 171.641 56	32	1.5	NaN	+	f	A4Pi	13	1	−0.5	0.5
1478	20 197.234 09	32	1.5	NaN	+	f	A4Pi	13	1	0.5	1.5
1479	20 262.645 13	32	1.5	NaN	+	f	B4Pi	9	1	−1.5	−0.5
1480	20 317.014 79	32	1.5	NaN	+	f	B4Pi	9	1	−0.5	0.5
1481	20 379.261 76	32	1.5	NaN	+	f	B4Pi	9	1	0.5	1.5
1482	20 468.803 76	32	1.5	NaN	+	f	a2Sigma−	16	0	0.5	0.5

Column	Notation	
1	n	Energy level reference number (row)
2	$\tilde{E}$	Term value (in cm^{-1})
3	g_{tot}	Total degeneracy
4	J	Rotational quantum number
5	τ	Radiative lifetime
6	$+/-$	Total parity
7	e/f	Rotationless parity
8	State	Electronic state
9	v	State vibrational quantum number
10	Λ	Projection of the electronic angular momentum
11	Σ	Projection of the electronic spin
12	Ω	$>\Omega = \Lambda + \Sigma$ (projection of the total angular momentum)

using the standard ExoMol format (Tennyson, Hill & Yurchenko 2013; Tennyson et al. 2016b). Extracts from the start of the $^{51}V^{16}O$ files are given in Table 15 (the states file) and Table 16 (the transition file). The full line list are available online.[1] The line list and partition functions together with the auxiliary data including the potential parameters and dipole moment functions, as well as the absorption spectrum given in cross-section format (Hill, Yurchenko & Tennyson 2013), can all be obtained from www.exomol.com.

3.3 Partition function

The partition function for $^{51}V^{16}O$ was calculated by summing all the calculated energy levels given by the DUO calculation up to both $J = 200.5$ and 270.5. The partition function is increased by 0.34 per cent at 5000 K for the latter more thorough calculation; this indicates convergence of the partition function from our model with respect to increased number of energy levels. These results are compared with the result of Sauval & Tatum (1984) and Barklem & Collet (2016) in Table 17. Both these previous results rely on data from Huber & Herzberg (1979). There are significant differences between the two literature values. Barklem & Collet agree much better with our new ExoMol data up to around 2000 K, while Sauval & Tatum are closer at the very high temperature range. In both cases, the partition function from the VOMYT spectroscopic model is significantly different from the pre-existing partition functions and should be used in preference to either of the former. Note that the VOMYT partition function relies primarily on the PECs, one of the most well-known aspects of the VO spectroscopic model due to the availability of significant experimental data. This gives higher reliability to our partition function.

[1] The full line list can be downloaded from the CDS, via ftp://cdsarc.u-strasbg.fr/pub/cats/J/MNRAS/xxx/yy, or http://cdsarc.u-strasbg.fr/viz-bin/qcat?J/MNRAS//xxx/yy or www.exomol.com

Table 16. Extract from the transition file for $^{51}V^{16}O$.

F	*I*	A_{IF} / s^{-1}
881	23	8.8193E−09
641	23	6.1704E−03
544	23	8.5161E−04
761	23	5.6700E−03
882	23	1.5569E−09
642	23	1.4461E+02
545	23	1.9240E−11
762	23	5.1683E−08
883	23	6.8306E−12
643	23	1.5453E−08
546	23	3.3650E−04
763	23	1.1708E−08
884	23	4.1096E−12
644	23	1.1716E−07
547	23	2.3980E−02
764	23	3.5896E−09
885	23	1.0346E−03

Notes. F: upper state counting number.
I: lower state counting number.
A_{IF}: Einstein *A* coefficient in s^{-1}.

Table 17. Partition function, $Q(T)$, for $^{51}V^{16}O$, as a function of temperature. The literature partition function are multiplied by the nuclear degeneracy factor (8) to match ExoMol's standard definitions.

T/K	VOMYT Final states	VOMYT Up to $J =$ 270.5	Sauval & Tatum (1984)	Barklem & Collet (2016)
0	16.0			
10	314.5			417.8
20	691.0			824.8
50	1888.3			2045.9
100	3915.2			4081.6
300	12 159.9			12 332.3
500	21 428.4			21 608.9
1000	53 462.1	53 462.1	72 288.9	53 665.6
1500	100 352.2	100 352.1	142 806.4	100 104.8
2000	165 542.6	165 542.0	237 928.8	161 561.6
3000	384 291.3	384 314.8	518 396.0	332 684.8
4000	808 962.6	809 705.9	951 848.0	
5000	1566 676.4	1573 175.4	1584 840.0	925 184.0
8000	7045 027.9	7293 154.8	5289 232.0	2859 736.0

3.4 Lifetimes

One important external check for our transition moments is the comparison of our lifetimes against experimental values. This is shown in Table 18. The ordering of lifetimes between the different electronic bands is definitely preserved, as is the rough order of magnitude of the result. However, there are discrepancies, particularly for the A–X transition. At this level, it is somewhat unclear whether this indicates errors in the *ab initio* or experimental results. There are certainly errors in the *ab initio* calculations, which we estimate to be approximately 10 per cent of the total value (McKemmish et al. 2016). However, there is no theoretical support for an approximately 40 per cent increase in the off-diagonal dipole moments which would be needed to bring the *ab initio* and Karlsson et al. (1997) experimental results into agreement. Therefore, we have decided to use pure *ab initio* values for all transition moments.

Table 18. Comparison of computed lifetimes, in μs, with the measurements of Karlsson et al. (1997).

	v	Karlsson et al. (1997)	VOMYT
$A\,^4\Pi_{5/2}$	0	7.0(4)	18.7
$A\,^4\Pi_{3/2}$	0	5.2(3)	19.1
$A\,^4\Pi_{1/2}$	0	5.3(3)	19.6
$A\,^4\Pi_{-1/2}$	0	5.7(5)	19.2
$B\,^4\Pi_{5/2}$	0	0.348(20)	0.823
$B\,^4\Pi_{5/2}$	1	0.328(22)	0.803
$B\,^4\Pi_{3/2}$	0	0.397(15)	0.838
$B\,^4\Pi_{3/2}$	1	0.380(18)	0.816
$B\,^4\Pi_{1/2}$	0	0.346(15)	0.851
$B\,^4\Pi_{1/2}$	1	0.420(35)	0.85
$B\,^4\Pi_{-1/2}$	0	0.406(18)	0.870
$B\,^4\Pi_{-1/2}$	1	0.50(6)	1.16
$C\,^4\Sigma^-$	0	0.073(2)	0.103
$C\,^4\Sigma^-$	1	0.063(4)	0.103

Further lifetimes measurements would be much appreciated to help resolve these discrepancies.

4 COMPARISONS

Fig. 8 compares the A–X 0–0 band in the region 9420–9560 cm^{-1} as observed by Cheung et al. (1982b) against a cross-section produced with our new line list using ExoCross LTE emission at 1000 K, with HWHM = 0.03 cm^{-1}. It is clear that the bandhead is very well reproduced (within 0.01 cm^{-1}). The general structure of the rest of the region is good, though not perfect.

The top plot in Fig. 9 shows the spectra of M-type stars between 0.46 and 0.64 μm (15 600–22 000 cm^{-1}) against the new VO ExoMol line list and the pre-existing TiO line list by Kurucz. The bottom plot is a zoomed-in view of the region from 0.56 to 0.61 μm (16 400–17 900 cm^{-1}). The absorption by VO in this spectral region is dominated by the C–X transition bandheads. The top plot shows clearly that the main bandheads observed in the M-star spectra arise from TiO, not VO; this is expected as TiO is about an order of magnitude more abundant than VO. However, at approximately 0.548, 0.574 and 0.609 μm, the VO bandheads become strong while there are weak or non-existent nearby TiO bandheads. In this regions, spectral absorption features in the M-type spectra do align well with the strong VO bandheads. This is further confirmed by the depth of this absorption feature as the spectral class changes from early M-type to late M-type stars (top to bottom). The absorption feature is significantly more pronounced for the cooler star. This aligns with the fact that late M-type stars have more VO than early M-type stars (in fact, the presence of VO absorption bands is one of the characterizing spectral features of late M-type stars).

Fig. 10 compares the cross-section in the B–X region from the new VOMYT line list against stellar spectra. The top plot is the B–X 1–0 band in the region 0.72–0.77 μm (12 990–13 890 cm^{-1}). Note that the M-star spectra are total cross-section, including a blackbody contribution that rises steeply in this spectral region, whereas the ExoMol cross-section is a pure absorption spectra on a fixed intensity background. It is expected that the M8 star contains significant VO absorption features which are weak or non-existent in the M4 spectra. This is indeed what is observed. The agreement in the region 0.73–0.75 μm is particularly strong. This corresponds to the B–X 1–0 band. The blackbody background is probably responsible for at least some of the differences from 0.75 to 0.758 μm, while the

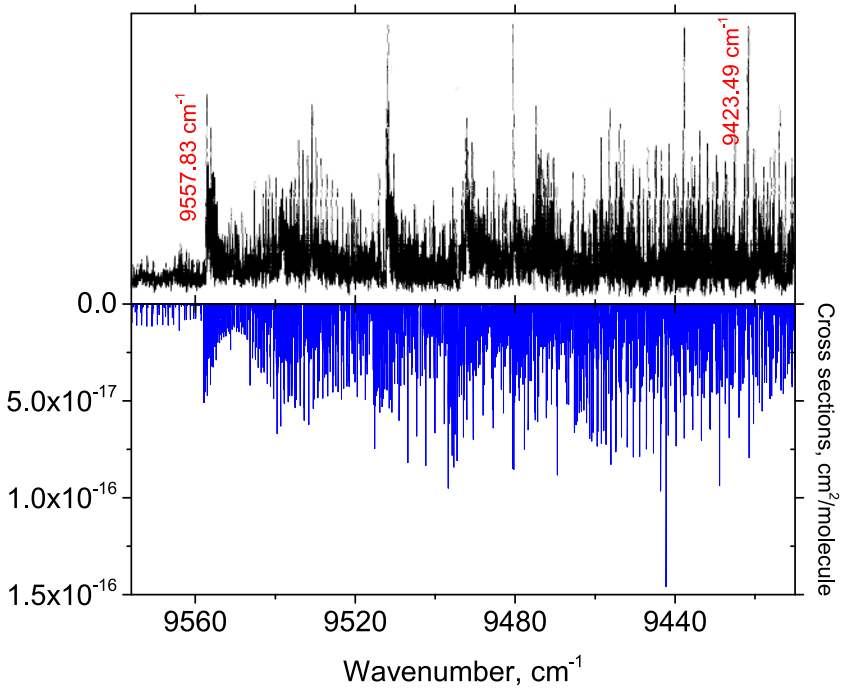

Figure 8. Comparison of VO X–A band (bottom panel) against laboratory spectra (top panel).

difference in the 0.758–0.764 μm is probably caused by absorption by another molecule.

The middle plot is the 0–0 band, centred around 0.79 μm (12 660 cm^{-1}). This figure compares the VO ExoMol cross-section against the spectra of a late M-type star in the region 0.783–0.81 μm (12 770–12 350 cm^{-1}). The absorption peaks in the stellar spectra and the VOMYT cross-section are extremely similar, giving high confidence to our VOMYT line list.

Finally, the bottom plot of Fig. 10 is the B–X 0–1 band with origin around 0.862 μm. This figure compares the VOMYT cross-section at 3000 K against the spectra of a M7 and M8 star in the region 0.844–0.890 μm (11 230–11 850 cm^{-1}). Some features clearly align between the VOMYT and stellar spectra, as indicated by the vertical lines.

Fig. 11 compares the VOMYT VO cross-section against stellar spectra in the region of the A–X 0–1 (top), 0–0 (middle) and 1–0 (bottom) bands. Considering first the middle subplot (the 0–0 band). The first major peak in the VO cross-section at around 1.046 μm aligns well with a bump in the M9 spectral absorption, though there is obviously another species causing a nearby strong absorption at 1.046 μm. The other peaks of the VO spectra all align reasonably well or at least are not inconsistent with the M9 stellar spectra, though there is again many other absorption peaks in this region. Note that the M2 and M3 stellar spectra seem reasonably featureless in this region and their absorption features do not coincide with VO's (as expected). The M2 and M3 absorption features do seem roughly correlated with some other absorption in the M9 stellar spectra.

The top subplot of Fig. 11 covers the 0–1 band region and shows similar characteristics to the 0–0 band; the VOMYT absorption features are present in (or consistent with) the M9 but not the M2/M3 spectra and there are many other absorption features in the M9 and M2/M3 spectra that do not arise from VO absorption, but probably a different molecule.

The bottom subplot of Fig. 11 covers the VO 1.2 μm band. There is little experimental data on the vibrationally excited A $^4\Pi$ state (only a tentative assignment of the vibrational frequency). Despite this, the agreement between the stellar spectra and the VO line list is reasonably good. The shape of the band is well reproduced and identification of the spectral features that can be attributed to VO are relatively clear. However, the positions of the spectral lines is somewhat in error (on order of 10 Å, around 10 cm^{-1}). This is about the expected error of this band and is a good indicator of the quality of this line list where direct experimental frequency measurements are not available, e.g. many hot and overtone bands.

Thus, our comparisons in Figs 9–11 show that the VO absorption features from our ExoMol cross-sections are consistent in the major bands to absorption in the late M-type stars, while VO absorption features are absent in the early M-type stars, as expected.

The characteristics of the Kurucz (2011), Plez (1999) and new ExoMol VOMYT line lists are summarized in Table 19. Note that even though the Kurucz line list has very low frequency transitions, all transitions are electronic; the infrared rovibrational transitions within the X state are not included. It is clear that the new VOMYT line list is significantly more complete, with more than 60 times more lines covering both shorter and longer wavelengths than either of the previous line lists. There are more electronic states considered, and more vibrational energy levels. The maximum rotational quantum number J is slightly lower due to the fact we used a lower energy cut-off to exclude all spectral lines originating from initial energies greater than 20 000 cm^{-1}.

Use of our partition function suggests that the Kurucz and Plez line lists are 90 per cent complete at 2800 K, but fall to approximately 50 per cent complete by 5000 K. This incompleteness means that for high temperatures significant sources of opacity will be missing. The Plez line list has used extensively in models of hot Jupiters, brown dwarfs and cold stars, e.g. by Plez (1999) as well as within the MARCS (Gustafsson et al. 2008), PHOENIX (Jack, Hauschildt & Baron 2009) and VSTAR (Bailey & Kedziora-Chudczer 2012) modelling programs.

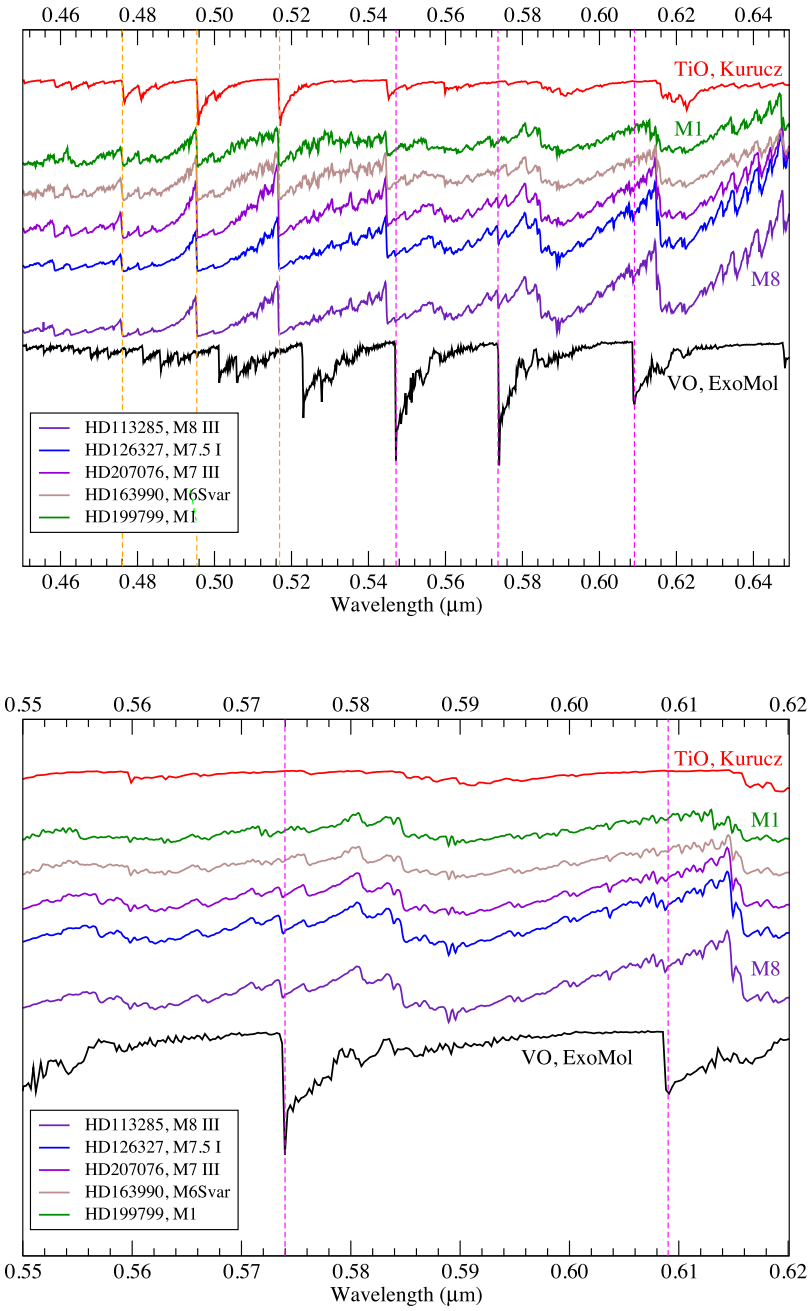

Figure 9. Comparison of VO spectra against stars of M stellar class (in legend) in the region of the C–X bands. Astronomical data are taken from the MILES stellar library of Sánchez-Blázquez et al. (2006) and Falcón-Barroso et al. (2011). Vertical lines indicate bandheads. For both panels, the stars from top to bottom are HD199799 (M1), HD163990 (M6Svar), HD207076 (M7III), HD12327 (M7.5 I) and HD113285, M8III).

Fig. 12 compares the Plez, Kurucz and ExoMol VOMYT line lists in the regions 0.3 and 5 μm. It is clear that the three line lists are broadly similar shorter than about 2 μm, though the ExoMol VOMYT line list extends to shorter wavelengths (and thus more to the blue). However, there are noticeable differences in intensities. For the A–X bands around 1 μm, the Kurucz line list is significantly stronger than either the Plez or ExoMol VOMYT line lists. The three line lists have similar strengths around the B–X bands, though the ExoMol line list is generally strongest especially at regions far from the bandhead; this is expected as it is most complete. The ExoMol VOMYT line list has stronger transitions in the C–X bands than either the Kurucz or Plez line lists.

Looking to the longer wavelength regions, the Plez line list does not represent the region longer than 2 μm well. The Kurucz line list is better with some features, but the ExoMol VOMYT line list is significantly more complete. This is because the ExoMol line list for the first time includes transitions from other electronic states, and from excited electronic states. The additional infrared absorption of VO described by our new line list may be important for energy transport and the spectroscopy of stellar and planetary atmospheres which contain VO molecule.

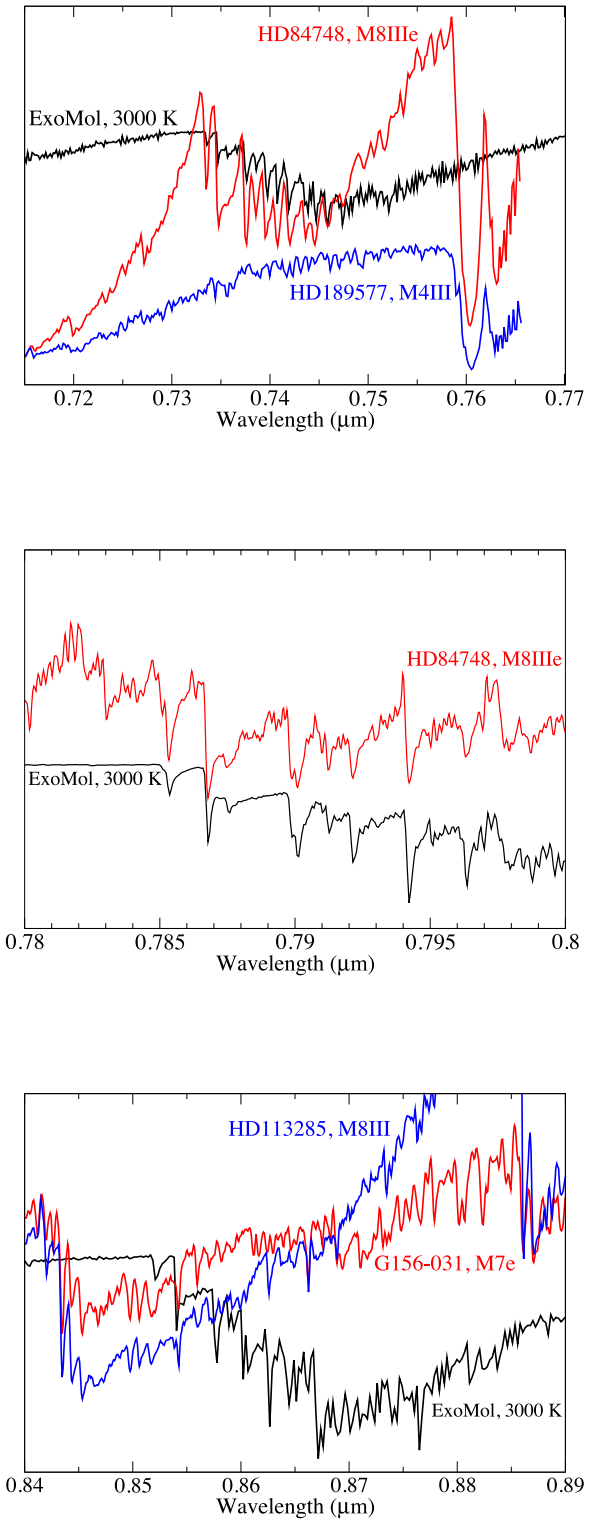

Figure 10. Comparison of VO spectra against stars of M stellar class (in legend) in the region B–X 1–0 (top), 0–0 (middle) and 0–1 (bottom) bands. Astronomical data are taken from the MILES stellar library by Sánchez-Blázquez et al. (2006), Falcón-Barroso et al. (2011) for the top two panels and from CaT stellar library from Cenarro et al. (2001) for the bottom panel. Vertical lines indicate VO bandheads.

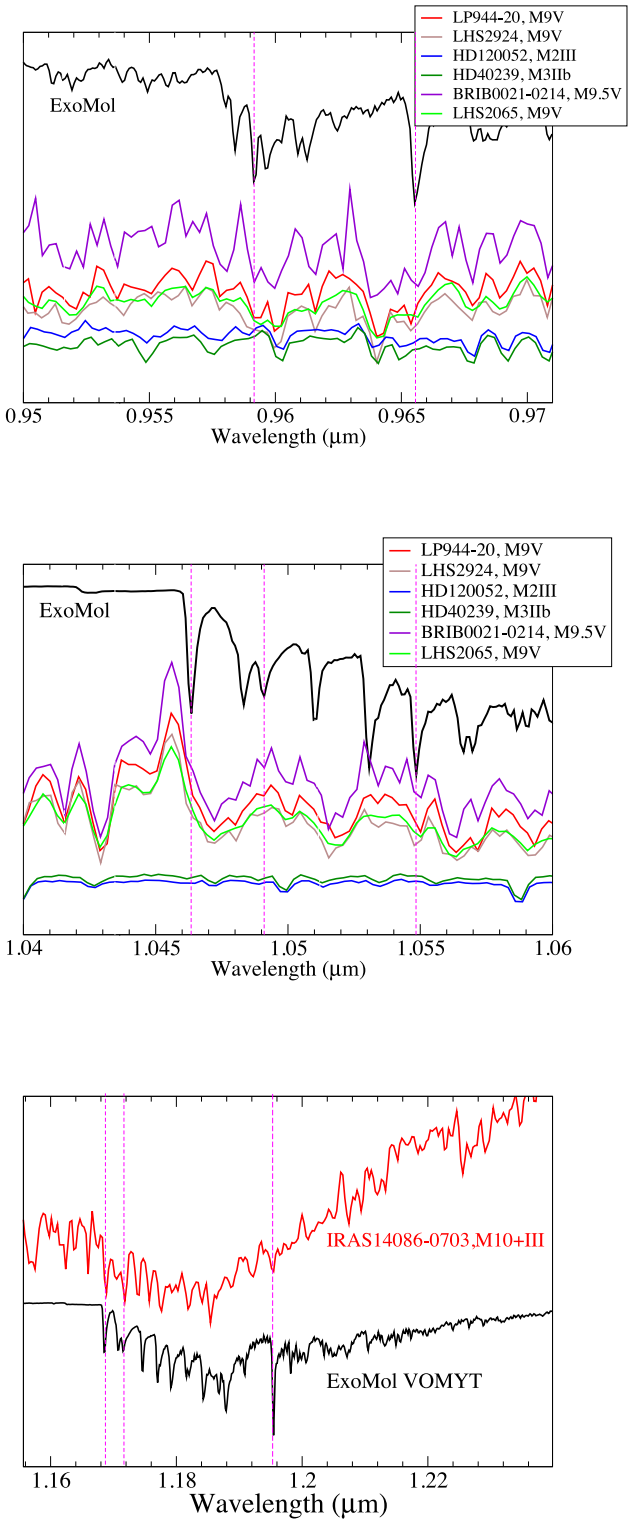

Figure 11. Comparison of VO spectra against stars of M stellar class (in legend) in the region of A–X bands. Astronomical data is taken from Rayner, Cushing & Vacca (2009). Vertical lines indicate VO bandheads. For the top two panels, the stellar curves from top to bottom are BRIB0021-0214 (M9.5V), LP944-20 (M9V), LHS2065 (M9V), LHS2929 (M9V), HD40239 (M3IIb) and HD120052 (M2III).

Table 19. Summary of available VO line lists.

	Plez (1999)	Kurucz (2011)	VOMYT
# Electronic states	4	4	13
Max v	15	15	59
Max J	199.5	199.5	197.5
Max energy (cm^{-1})	42 387		50 000
Min freq. (cm^{-1})	3 767	0.537	0.01
Max freq. (cm^{-1})	25 939	28 096	35 000
Min wavelength (μm)	0.386	0.355	0.2857
Max wavelength (μm)	2.655	18 627.4	1000 000
Number of lines	3171 552	4509 519	277 131 624

Fig. 13 identifies the main bands in the absorption spectra of VO at 2200 K. The strongest microwave and infrared bands are about three orders of magnitude weaker than the strongest visible bands. In visible spectral region, the C–X transition has an inherently stronger intensity than the B–X transition, which is stronger than the A–X transition. It is clear that the A–X, B–X and C–X transitions contribute almost all of the opacity above 7000 cm^{-1} (below 1.4 μm). At low frequencies (longer wavelengths), there are a significant number of contributing transitions, particularly the e–c, B–A and X–X transitions.

The importance of these non-ground electronic states can be quantified by considering the thermal distribution of initial states in an ensemble of VO molecules. Fig. 14 shows the relative population of excited states as a function of temperature. At 2000 K, only 2 per cent of molecules are in excited states; by 5000 K, this increases to almost 45 per cent! Furthermore, there are many excited states that are populated significantly; though the A′ state have the highest population (15 per cent), there is significant population (above 1 per cent) in six other excited states.

Our calculated transitions associated with the ground state will generally be more reliable than transitions that occur between excited states. This is due to existing experimental data. For example, T_e for the a $^2\Sigma^-$ state is not well known experimentally and thus the frequencies of all transitions from this state have inherent large uncertainties. Limitations in the accuracy of the *ab initio* calculations also needs to be considered; low lying states are generally described more accurately than higher electronic states.

Fig. 15 shows the absorption spectra as a function of temperature. At higher temperatures, the structure of the spectra becomes less defined and broader, as expected.

5 CONCLUSION

Transition metal diatomics are important species in cooler stars and hot Jupiters. However, the difficulty of the *ab initio* calculations and the relative lack of experimental data mean that it is difficult to construct high-quality line lists for these species.

Here we present the first ExoMol line list for a transition metal diatomic species of astrophysical relevance. Work on CrH, MnH and TiH is in advanced stages and will be published shortly. Using the lessons from the construction of the VO line list, we are now actively working on an improved high-quality line list for TiO to address much discussed shortcomings in the existing line list in terms of intensities and at very high resolution. This new TiO line list will use high-quality *ab initio* results and be fitted to all available experimental data. Furthermore, a MARVEL-type analysis (Furtenbacher et al. 2007) is currently underway to extract high-quality experimental energies from experimental frequencies.

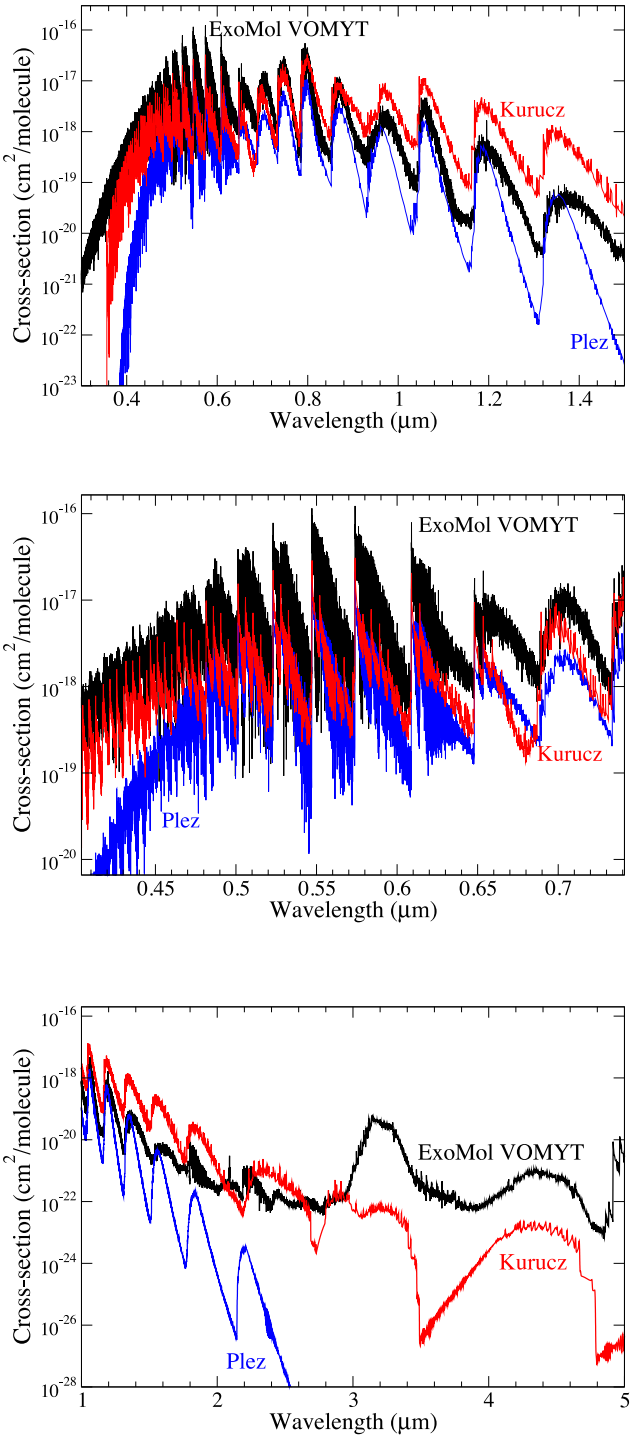

Figure 12. Comparison between the Plez, Kurucz and new ExoMol VOMYT line lists for VO. All cross-sections are obtained at 2200 K and using a HWHM of 1 cm^{-1}.

Our VOMYT rovibronic line list for VO, containing over 277 million transitions, can be accessed online at www.exomol.com in the extended ExoMol format described by Tennyson et al. (2016b). It includes the transition energies and Einstein coefficients, partition functions, lifetimes and temperature-dependent cross-sections. Landé g factors to describe the splitting of the energy levels due to

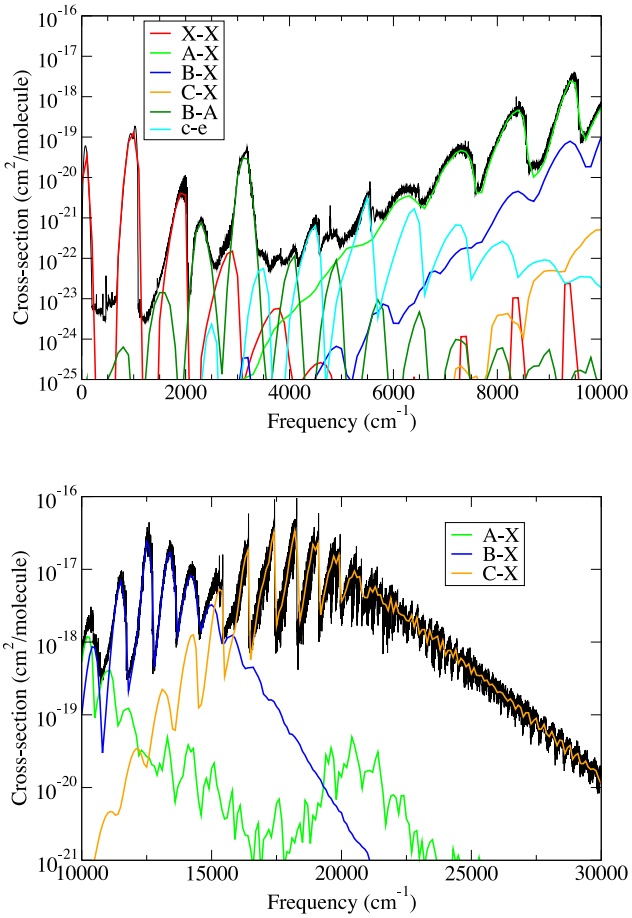

Figure 13. Decomposition of the total cross-section of VO below 30 000 cm^{-1} into the main bands. HWHM = 1 cm^{-1}, T = 2200 K. In the top panel, the X–X transition is responsible for the first three main peaks. The A–X transition is responsible for all peaks from 6000 to 10 000 cm^{-1}. The c–e transition produces peaks at around 4500 and 5500 cm^{-1}. The B–X transition peaks around 2300 and 3100 cm^{-1}. The C–X and B–X transitions are weak below 10 000 cm^{-1} and do not contribute significantly to the absorption. In the bottom panel, the curve peaking at around 10 000 cm^{-1} is for the A–X band, the curves peaking between 10 000 and 15 000 cm^{-1} is the B–X band and the curve peaking from 15 000 to 25 000 cm^{-1} is the C–X band.

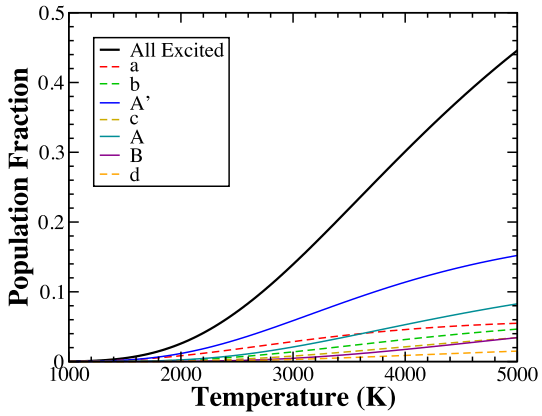

Figure 14. Relative population of excited states (where full population is normalized to 1). At 5000 K, the lines from top to bottom refer to All excited states, A', A, a, b, B, c and d states. The solid lines are quartet states, while the dotted lines are doublet states.

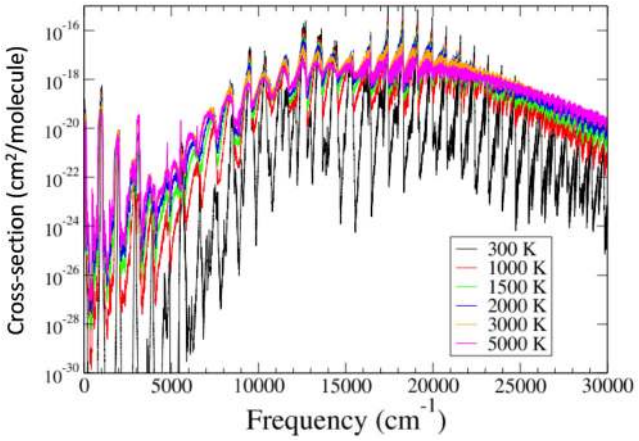

Figure 15. Overview of the full spectrum of VO for T = 300, 1000, 2000, 3000 and 5000 K, absorption cross-sections (cm^2 molecule^{-1}) with HWHM = 1 cm^{-1}. Looking at the minimum of the spectra, the cross-sections are ordered in increasing temperature.

the Zeeman effect will be added shortly. We have also included the DUO input file with our spectroscopic model for VO.

ACKNOWLEDGEMENTS

This work is supported by ERC Advanced Investigator Project 267219. The authors acknowledge the use of the UCL Legion High Performance Computing Facility (Legion@UCL), and associated support services, in the completion of this work. Thanks to Joanna Barstow, Adam Burgasser, Jane MacArthur, August Muench and Hannah Wakeford for recommending good sources of astronomical data to compare against our line list's predictions.

REFERENCES

Adam A. G., Barnes M., Berno B., Bower R. D., Merer A. J., 1995, J. Mol. Spectrosc., 170, 94
Agúndez M., Parmentier V., Venot O., Hersant F., Selsis F., 2014, A&A, 564, A73
Allard F., Hauschildt P. H., 1995, ApJ, 445, 433
Alvarez R., Plez B., 1998, A&A, 330, 1109
Bailey J., Kedziora-Chudczer L., 2012, MNRAS, 419, 1913
Bakalbassis E. G., Stiakaki M. A. D., Tsipis A. C., Tsipis C. A., 1996, Chem. Phys., 205, 389
Balabanov N. B., Peterson K. A., 2005, J. Chem. Phys., 123, 064107
Balducci G., Gigli G., Guido M., 1983, J. Chem. Phys., 79, 5616
Bande A., Lüchow A., 2008, Phys. Chem. Chem. Phys., 10, 3371
Barklem P. S., Collet R., 2016, A&A, 588, A96
Barstow J. K., Aigrain S., Irwin P. G. J., Kendrew S., Fletcher L. N., 2015, MNRAS, 448, 2546
Bauschlicher C. W., Langhoff S. R., 1986, J. Chem. Phys., 85, 5936
Bauschlicher C. W., Maitre P., 1995, Theor. Chim. Acta, 90, 189
Beichman C. et al., 2014, PASP, 126, 1134
Bernath P. F., 2009, Int. Rev. Phys. Chem., 28, 681
Bowler B. P., Liu M. C., Dupuy T. J., Cushing M. C., 2010, ApJ, 723, 850
Bridgeman A. J., Rothery J., 2000, J. Chem. Soc. Dalton, 211
Broclawik E., Borowski T., 2001, Chem. Phys. Lett., 339, 433
Burrows A., Hubbard W., Lunine J. I., 1989, ApJ, 345, 939
Carlson K. D., Moser C., 1966, J. Chem. Phys., 44, 3259
Castelaz M., Luttermoser D., Piontek R., 2000, ApJ, 538, 341
Cenarro A., Cardiel N., Gorgas J., Peletier R., Vazdekis A., Prada F., 2001, MNRAS, 326, 959
Cheung A. S. C., Hansen R. C., Lyyra A. M., Merer A. J., 1981, J. Mol. Spectrosc., 86, 526

Cheung A. S. C., Hansen R. C., Merer A. J., 1982a, J. Mol. Spectrosc., 91, 165
Cheung A. S. C., Taylor A. W., Merer A. J., 1982b, J. Mol. Spectrosc., 92, 391
Cheung A. S. C., Hajigeorgiou P. G., Huang G., Huang S. Z., Merer A. J., 1994, J. Mol. Spectrosc., 163, 443
Dai B., Deng K., Yang J., Zhu Q., 2003, J. Chem. Phys., 118, 9608
Désert J.-M., Vidal-Madjar A., Lecavelier des Etangs A., Sing D., Ehrenreich D., Hébrard G., Ferlet R., 2008, A&A, 492, 585
Dolg M., Wedig U., Stoll H., Preuss H., 1987, J. Chem. Phys., 86, 2123
Dunning T. H., 1989, J. Chem. Phys., 90, 1007
Evans T. M. et al., 2016, ApJ, 822, L4
Falcón-Barroso J., Sánchez-Blázquez P., Vazdekis A., Ricciardelli E., Cardiel N., Cenarro A., Gorgas J., Peletier R., 2011, A&A, 532, A95
Fortney J. J., Lodders K., Marley M. S., Freedman R. S., 2008, ApJ, 678, 1419
Fortney J. J., Shabram M., Showman A. P., Lian Y., Freedman R. S., Marley M. S., Lewis N. K., 2010, ApJ, 709, 1396
Furtenbacher T., Császár A. G., Tennyson J., 2007, J. Mol. Spectrosc., 245, 115
Gibson N. P., Aigrain S., Barstow J. K., Evans T. M., Fletcher L. N., Irwin P. G. J., 2013, MNRAS, 436, 2974
Gustafsson B., Edvardsson B., Eriksson K., Jorgensen U. G., Nordlund A., Plez B., 2008, A&A, 486, 951
Harrington J., Nicholls R. W., 1969, J. R. Astron. Soc. Can., 63, 208
Haynes K., Mandell A. M., Madhusudhan N., Deming D., Knutson H., 2015, ApJ, 806, 146
Herczeg G. J., Hillenbrand L. A., 2014, ApJ, 786, 97
Hill C., Yurchenko S. N., Tennyson J., 2013, Icarus, 226, 1673
Hocking W. H., Merer A. J., Milton D. J., 1981, Can. J. Phys., 59, 266
Hoeijmakers H. J., de Kok R. J., Snellen I. A. G., Brogi M., Birkby J. L., Schwarz H., 2015, A&A, 575, A20
Hopkins W. S., Hamilton S. M., Mackenzie S. R., 2009, J. Chem. Phys., 130, 144308
Huang G. I., Merer A. J., Clouthier D. J., 1992, J. Mol. Spectrosc., 153, 32
Huber K. P., Herzberg G., 1979, Molecular Spectra and Molecular Structure IV. Constants of Diatomic Molecules. Van Nostrand Reinhold Company, New York
Hübner O., Hornung J., Himmel H.-J., 2015, J. Chem. Phys., 143, 024309
Huitson C. M., Sing D. K., Vidal-Madjar A., Ballester G. E., Lecavelier des Etangs A., Désert J.-M., Pont F., 2012, MNRAS, 422, 2477
Jack D., Hauschildt P. H., Baron E., 2009, A&A, 502, 1043
Karlsson L., Lindgren B., Lundevall C., Sassenberg U., 1997, J. Mol. Spectrosc., 181, 274
Kasai P. H., 1968, J. Chem. Phys., 49, 4979
Keenan P. C., Schroeder L. W., 1952, ApJ, 115, 82
Kirkpatrick J. D., Kelly D. M., Rieke G. H., Liebert J., Allard F., Wehrse R., 1993, ApJ, 402, 643
Kirkpatrick J. D., Barman T. S., Burgasser A. J., McGovern M. R., McLean I. S., Tinney C. G., Lowrance P. J., 2006, ApJ, 639, 1120
Knowles P. J., Werner H.-J., 1988, Chem. Phys. Lett., 145, 514
Knowles P. J., Werner H.-J., 1992, Theor. Chem. Acc., 84, 95
Kuiper G. P., Wilson W., Cashman R. J., 1947, ApJ, 106, 243
Kulik H. J., Marzari N., 2010, J. Chem. Phys., 133, 114103
Kurucz R. L., 2011, Can. J. Phys., 89, 417
Laud B. B., Kalsulka D. R., 1968, Indian J. Phys., 42, 61
Lee E. G., Seto J. Y., Hirao T., Bernath P. F., Le Roy R. J., 1999, J. Mol. Spectrosc., 194, 197
Lodi L., Yurchenko S. N., Tennyson J., 2015, Mol. Phys., 113, 1559
Mackrodt W. C., Middlemiss D. S., Owens T. G., 2004, Phys. Rev. B, 69, 115119
Madhusudhan N., Seager S., 2010, ApJ, 725, 261
McGovern M. R., Kirkpatrick J. D., McLean I. S., Burgasser A. J., Prato L., Lowrance P. J., 2004, ApJ, 600, 1020
McKemmish L. K., Yurchenko S. N., Tennyson J., 2016, Mol. Phys., in press, doi:10.1080/00268976.2016.1225994
Merer A., 1989, Annu. Rev. Phys. Chem., 40, 407
Merer A. J., Huang G., Cheung A. S. C., Taylor A. W., 1987, J. Mol. Spectrosc., 125, 465
Miliordos E., Mavridis A., 2007, J. Phys. Chem. A, 111, 1953
Parmentier V., Showman A. P., Lian Y., 2013, A&A, 558, A91
Patrascu A. T., Hill C., Tennyson J., Yurchenko S. N., 2014, J. Chem. Phys., 141, 144312
Patrascu A. T., Tennyson J., Yurchenko S. N., 2015, MNRAS, 449, 3613
Peterson D. E. et al., 2008, ApJ, 685, 313
Plez B., 1998, A&A, 337, 495
Plez B., 1999, in Le Bertre T., Lebre A., Waelkens C., eds, Proc. IAU Symp. 191, Asymptotic Giant Branch Stars. Springer Science & Business Media, New York, p. 75
Pradhan K., Gutsev G. L., Weatherford C. A., Jena P., 2011, J. Chem. Phys., 134, 144305
Pykavy M., van Wullen C., 2003, J. Phys. Chem. A, 107, 5566
Quan D., Ling W., Xiao-Hong S., Tao G., 2006, Acta Phys. Sin., 55, 6308
Quan D., Ling W., Xiao-Hong S., Hong-Yan W., Tao G., Zheng-He Z., 2008, Acta Chim. Sin., 66, 23
Rajpurohit A. S., Reylé C., Schultheis M., Allard F., Scholz R., Homeier D., 2012, in Boissier S., de Laverny P., Nardetto N., Samadi R., Valls-Gabaud D., Wozniak H., eds, SF2A-2012: Proc. Annual Meeting of the French Society of Astronomy and Astrophysics. Societe Francaise d'Astronomie et d'Astrophysique, p. 383
Rajpurohit A. S., Reylé C., Allard F., Scholz R. D., Homeier D., Schultheis M., Bayo A., 2014, A&A, 564, A90
Ram R. S., Bernath P. F., 2005, J. Mol. Spectrosc., 229, 57
Ram R. S., Bernath P. F., Davis S. P., Merer A. J., 2002, J. Mol. Spectrosc., 211, 279
Rayner J. T., Cushing M. C., Vacca W. D., 2009, ApJS, 185, 289
Richards D., Barrow R. F., 1968a, Nature, 219, 1244
Richards D., Barrow R. F., 1968b, Nature, 217, 842
Ryabchikova T., Piskunov N., Kurucz R. L., Stempels H. C., Heiter U., Pakhomov Y., Barklem P. S., 2015, Phys. Scr., 90, 054005
Sánchez-Blázquez P. et al., 2006, MNRAS, 371, 703
Sauval A. J., Tatum J. B., 1984, ApJS, 56, 193
Schwarz H., Brogi M., de Kok R., Birkby J., Snellen I., 2015, A&A, 576, A111
Schwenke D. W., 1998, Faraday Discuss., 109, 321
Sharp C. M., Burrows A., 2007, Astrophys. J. Suppl. Ser., 168, 140
Spiegel D. S., Burrows A., 2013, ApJ, 772, 76
Spiegel D. S., Silverio K., Burrows A., 2009, ApJ, 699, 1487
Spinrad H., Wing R. F., 1969, ARA&A, 7, 249
Spinrad H., Younkin R. L., 1966, PASP, 78, 65
Sriramachandran P., Bagare S. P., Rajamanickam N., Balachandrakumar K., 2008, Sol. Phys., 252, 267
Suenram R. D., Fraser G. T., Lovas F. J., Gillies C. W., 1991, J. Mol. Spectrosc., 148, 114
Šurkus A. A., Rakauskas R. J., Bolotin A. B., 1984, Chem. Phys. Lett., 105, 291
Tennyson J., 2014, J. Mol. Spectrosc., 298, 1
Tennyson J., Yurchenko S. N., 2012, MNRAS, 425, 21
Tennyson J., Yurchenko S. N., 2014, in Cami J., Cox N. L. J., eds, Proc. IAU Symp. 297, The Diffuse Interstellar Bands. Cambridge Univ. Press, Cambridge, p. 330
Tennyson J., Yurchenko S., 2016, Exp. Astron., 40, 563
Tennyson J., Hill C., Yurchenko S. N., 2013, in Gillaspy J. D., Wiese W. L., Podpaly Y. A., eds, AIP Conf. Ser. Vol. 1545, Eighth International Conference on Atomic and Molecular Data and their Applications: ICAMDATA-2012. Am. Inst. Phys., New York, p. 186
Tennyson J., Lodi L., McKemmish L. K., Yurchenko S. N., 2016a, J. Phys. B: At. Mol. Opt. Phys., 49, 102001
Tennyson J. et al., 2016b, J. Mol. Spectrosc., in press, https://arxiv.org/abs/1603.05890
Tinetti G. et al., 2011, in Sozzetti A., Lattanzi M., Boss A., eds, Proc. IAU Symp. Ser. 276, The Astrophysics of Planetary Systems: Formation, Structure, and Dynamical Evolution. Cambridge Univ. Press, Cambridge, p. 359

Tinetti G. et al., 2012, Exp. Astron., 34, 311
Wakeford H. R., Sing D. K., 2015, A&A, 573, A122
Werner H., Knowles P. J., 1988, J. Chem. Phys., 89, 5803
Werner H.-J., Knowles P. J., Knizia G., Manby F. R., Schütz M., 2012, WIREs Comput. Mol. Sci., 2, 242
Western C. M., 2016, J. Quant. Spectrosc. Radiat. Transfer, in press, doi:10.1016/j.jqsrt.2016.04.010
Wing R. F., Spinrad H., Kuhi L., 1967, ApJ, 147, 117
Wolf G. V., Farberov D. S., Shirokovskii V. P., 1977, Int. J. Quantum Chem., 12, 485
Wu H. B., Wang L. S., 1998, J. Chem. Phys., 108, 5310
Yao C., Guan W., Song P., Su Z. M., Feng J. D., Yan L. K., Wu Z. J., 2007, Theor. Chem. Acc., 117, 115
Yurchenko S. N., Blissett A., Asari U., Vasilios M., Hill C., Tennyson J., 2016a, MNRAS, 456, 4524
Yurchenko S. N., Lodi L., Tennyson J., Stolyarov A. V., 2016b, Comput. Phys. Commun., 202, 262

SUPPORTING INFORMATION

Additional Supporting Information may be found in the online version of this article:

(http://www.mnras.oxfordjournals.org/lookup/suppl/doi:10.1093/mnras/stw1969/-/DC1).

Please note: Oxford University Press is not responsible for the content or functionality of any supporting materials supplied by the authors. Any queries (other than missing material) should be directed to the corresponding author for the article.

This paper has been typeset from a TEX/LATEX file prepared by the author.